Universidad Autónoma de Puebla
Instituto de Física "Luis Rivera Terrazas"

Estimation of the Hubble constant and Schwarzschild-de Sitter black hole parameters

Tesis presentada por

Déborah Elizabeth Villaraos Serés

para obtener el grado de

Maestra en Ciencias
(Física)

Dirigida por
Alfredo Herrera Aguilar
Mehrab Momennia

Puebla, México
Noviembre 2024

Acknowledgements

I would like to thank my advisor Dr. Alfredo Herrera for his constant support, patience, and guidance throughout my master's journey and in conducting this research. I am also grateful to my advisor Dr. Mehrab Momennia for his comments and his support in the preparation and writing of this thesis. To my thesis committee, Professors Gerardo Torres, Roberto Cartas and Siva Kumar, I appreciate their questions and valuable comments.

I thank CONAHCYT for providing me with financial support trough the Master grant No. 1071008.

I also thankfully acknowledge the computer resources, technical expertise and support provided by the Laboratorio Nacional de Supercómputo del Sureste de México (LNS), CONAHCYT member of the network of national laboratories.

Thanks to my colleague Dra. Adriana González, for her kind disposition and help. I am also thankful to MSc. Artemisa Villalobos for her help during the early stages of this research. I am also very grateful to Luis Rojas from IFUAP and Javier Tolentino from LNS for their invaluable help and guidance in understanding and utilizing the computer clusters.

I am also grateful to my master's classmates, especially Javier and Diana for their support and companionship throughout this journey. To Jhony for all these years of friendship, for always being there for me and for giving me academic and personal advice. To my friends Lore, Martín, Paola, and every person who offered me words of support. To Diego, for his constant encouragement and unconditional support, for his kindness and endless affection.

To my mom and dad, who have always supported me and encouraged me to keep going, for all their loving and advice. To my sister Xani, for always making me smile, for her unconditional support and for always rooting for me. To Cafi and Misha for providing me with emotional support and joy, for being the light of my life and my constant company night and days.

To Cafi

Estimación de la constante de Hubble y los parámetros de un agujero negro Schwarzchild-de Sitter

Resumen

En este trabajo de tesis utilizamos el fondo Schwarzschild-de Sitter, el cual describe un agujero negro estático y esféricamente simétrico en un universo dominado por la energía oscura. Obtenemos la expresión del corrimiento de fotones emitidos en la vecindad del agujero negro, cuya fuente orbita circularmente el agujero negro, y que son detectados por un observador lejano que tiene un movimiento de recesión debido a la expansión del universo. Tal expresión del corrimiento involucra cantidades observables, como el corrimiento de los fotones, así como parámetros del espacio-tiempo mismo, como la masa del agujero negro y la constante cosmológica. A continuación, aplicamos este modelo teórico a los sistemas de megamáseres de H_2O, que consisten en nubes de vapor de agua que emiten radiación en el espectro de las microondas y que se encuentran en el disco de acreción de agujeros negros. Utilizando observaciones astrofísicas del corrimiento al rojo y posición de estos máseres, realizamos una estimación estadística Bayesiana para encontrar los parámetros de masa, distancia y posición del agujero negro, así como de la constante de Hubble, por su relación con la constante cosmológica.

Estimation of the Hubble constant and Schwarzschild-de Sitter black hole parameters

Abstract

In this thesis, we work on the Schwarzschild-de Sitter background, which describes a static and spherically symmetric black hole immersed in a universe dominated by dark energy. We obtain the redshift expression of photons emitted by a massive particle circularly orbiting the black hole and detected by a far away observer with recessional movement due to the expansion of the universe. This redshift expression involves observable quantities, such as the redshift, with spacetime parameters, like the mass of the black hole and the cosmological constant. Thus, we apply this theoretical model to H_2O megamaser systems, which consist on water vapor clouds emitting radiation on the microwave regime, located on accretion disks of black holes. By using astrophysical observations of the redshift, blueshift and position of the maser features, we perform a Bayesian statistical fit to estimate the parameters of mass, distance and position of the black hole, as well as the value of the Hubble constant, through its relation to the cosmological constant.

Publications

- Déborah Villaraos, Alfredo Herrera-Aguilar, Ulises Nucamendi, Gustavo González-Juárez and Raúl Lizardo-Castro, "A general relativistic mass-to-distance ratio for a set of megamaser AGN black holes", *Monthly Notices of the Royal Astronomical Society*, Volume 517, Issue 3, Pages 4213–4219, (2022), arXiv:2207.06594 [astro-ph.GA].

Participation in events

- General relativistic mass-to-distance ratio for megamaser black holes, Déborah Villaraos, Alfredo Herrera-Aguilar, Ulises Nucamendi, Gustavo González-Juárez and Raúl Lizardo-Castro, Workshop on current aspects on Black Holes, Universidad Michoacana de San Nicolás Hidalgo, Morelia, México (2023).

- Agujeros negros en el IFUAP, Déborah Villaraos, Astrofísica para todos en el IFUAP, Benemérita Universidad Autónoma de Puebla, México (2023).

- A general relativistic mass-to-distance ratio for a set of megamaser AGN black holes, Déborah Villaraos, Alfredo Herrera-Aguilar and Ulises Nucamendi, Avances en Teoría de la Gravedad, Agujeros Negros y Cosmología, Universidad de Guanajuato, Guanajuato, México (2023).

- Black hole parameter estimation using Schwarzschild de Sitter redshift, Déborah Villaraos, Alfredo Herrera-Aguilar, Mehrab Momennia and Ulises Nucamendi, Simposio Estudiantil del Posgrado en Física IFUAP, Benemérita Universidad Autónoma de Puebla, México (2024).

- The Hubble constant and SdS black hole parameter estimation, Déborah Villaraos, Alfredo Herrera-Aguilar, Mehrab Momennia and Ulises Nucamendi, V Taller de Métodos Numéricos y Estadísticos en Cosmología, Instituto de Ciencias Físicas Universidad Nacional Autónoma de México, Cuernavaca, México (2024).

- Corrimiento al rojo de fotones alrededor de un agujero negro SdS, Déborah Villaraos, Alfredo Herrera-Aguilar, Mehrab Momennia and Ulises Nucamendi, XV Taller de la División de Gravitación y Física Matemática de la Sociedad Mexicana de Física, Universidad de Guanajuato, León, México (2024).

Content

Chapter 1

Introduction

In 1905, Einstein published the postulates of the special theory of relativity [1], establishing that the speed of light is constant for all observers in any inertial reference frame and that the laws of physics are identical for all observers within such frames. A decade later, he introduced the general theory of relativity [2, 3, 4], where he first presented the Einstein field equations. These equations describe how spacetime curvature is influenced by the presence of mass and energy, and in turn, how this curvature dictates the motion of particles. In this theory, gravity is not described as a force but rather as the result of spacetime curvature caused by mass, and particles follow geodesic paths within this curved spacetime.

A couple of months after the publication of this paper, Karl Schwarzschild found the first exact solution to Einstein's equations for the exterior of a static, spherically symmetric mass [5]. In subsequent years, general solutions for static objects were discovered, each incorporating different physical characteristics. These include the Reissner-Nordström metric for a charged mass [6, 7], or the Kottler metric, which introduces the cosmological constant to the Schwarzschild solution [8]. Friedrich Kottler proposed this metric after Einstein added the cosmological constant to his equations in order to obtain a static universe. However, in 1929, Edwin Hubble observed a relationship between the recession velocity of galaxies and their distance [9], leading to the conclusion that the universe is expanding. As a result, the original purpose of Einstein for adding the cosmological constant was reconsidered, and it is now used to describe an expanding universe, associated with the concept of dark energy in modern cosmology.

These early solutions to Einstein's equation predicted the existence of regions now understood as black holes. In [5], Schwarzschild identified a radius at which the escape velocity for a particle in this spacetime equals the speed of light; this critical distance, known as the Schwarzschild radius, describes the event horizon of the Schwarzschild black hole. Initially, the singularities in these solutions were considered purely mathematical with no physical meaning, as it was widely believed that a mass could not collapse below its Schwarzschild radius. However, physicists such as Chandrasekhar [10] and Oppenheimer [11] proposed mechanisms by which such gravitational collapse could occur, making plausible the existence of black holes. In the following years, the concept of black holes developed further, leading to a deeper understanding of these objects. The work of Penrose and Hawking [12, 13] demonstrated that singularities are natural consequences of general relativity, establishing black holes as extreme objects of the theory.

For decades, efforts to find astronomical evidence of black holes were unsuccessful and their existence remained speculative. The observation of accretion disks around massive compact objects in the X-ray regime provided indirect evidence supporting their presence [14, 15, 16]. However, it was not until nearly a century after the proposal of general relativity that compelling evidence was found by the detection of gravitational waves caused by the merger of two black holes, observed by the LIGO and Virgo collaborations [17, 18]. This discovery not only confirmed the existence of black holes as predicted by general relativity but also proved their dynamic behavior in the universe. Moreover, in recent years the Event Horizon Telescope collaboration provided the first images of black holes, capturing the shadow of the supermassive black hole at the core of the galaxy M87 and, shortly afterward, that of our own galaxy's central black hole, known as SgrA* [19, 20, 21, 22, 23].

Before this observational evidence, the existence of SgrA* was inferred through studies of the mass distribution in the central region of the Milky Way. Two research teams led by Andrea Ghez and Reinhard Genzel [24, 25, 26] studied the kinematics of stars at the center of our galaxy for decades, and independently determined the existence of a supermassive compact object with the mass of the order of 10^6 $M_\odot$ [27, 28, 29, 30]. Following this line of research, we are now interested in determining black hole parameters by studying the kinematics of objects lying in their accretion disk with the help of a different approach based on the frequency shift of the orbiting particles.

Some research papers on black holes use Newtonian analysis with relativistic corrections to find black hole parameters (see [31, 32, 33], for instance). However, since black holes are massive and compact, general relativity is the most adequate theory to describe them. Some general relativistic effects have no Newtonian analog, such as the gravitational redshift, the dragging effect of spacetime, and the gravitational lensing, among others [34, 35]. Hence, we use the general theory of relativity with its corresponding mathematical tools to relate astrophysical observables to the black hole parameters and spacetime properties.

In [36], a general relativistic model is described for a Kerr-de Sitter black hole orbited by a photon source. The photon source moves in circular orbits on the equatorial plane so that a distant observer located on the Earth observes the system edge-on. It is possible to find an expression for the frequency shift in terms of the mass and angular momentum of the black hole, the cosmological constant, and the test particle position by using the four-velocity of the test particle and the four-momentum of its emitted photons. This general relativistic approach has been applied to different metrics, see [34, 37, 38].

In this thesis, we use the Kottler solution, also known as the Schwarzschild-de Sitter (SdS) metric as a first approximation, without considering matter in our universe, given that this metric describes a static and spherically symmetric black hole immersed in an expanding universe dominated by dark energy. We obtain an expression for the redshift of photons in the vicinity of an SdS black hole in a similar manner as for the Kerr-de Sitter case, described in [36]. By using the SdS metric, we naturally introduce the rate of expansion of the universe H_0 in our equations through its relation to the cosmological constant Λ.

We aim to apply this theoretical model to actual astrophysical systems, specifically to the megamaser systems. These megamasers are vapor clouds found in the accretion disk of black holes at the core of active galactic nuclei (AGNs), stimulated by the black hole and emitting light in the microwave regime. Numerous observations of these systems show a thin disk seen edge-on from the Earth, with three groups of megamasers observed in the sky: the megamasers at the edges of the disk (where they are redshifted and blueshifted due to their rotation around the accretion disk) and the central megamasers [39]. According to literature, megamasers orbit a central mass around $10^6 - 10^7$ $M_\odot$, i.e., a mass of the order of a supermassive black hole. Moreover, they follow rotation curves with low eccentricity [40, 41]. Therefore, since megamaser systems constitute a thin accretion disk circularly orbiting a compact supermassive object, we can apply the aforementioned mathematical model for circular geodesic motion to these astrophysical systems, and look for evidence of general relativistic effects.

The Megamaser Cosmology Project is dedicated to discovering and observing megamaser systems at AGNs. They calculate the Hubble constant and the parameters of these black holes using Keplerian rotation curves with relativistic corrections [40, 41]. Their observations are available in public databases (e.g., [42, 43, 44]), thus, we use this public data to statistically estimate the black hole parameters using the general relativity formalism, as it was accomplished for several black holes in [45, 46, 47, 48]. Such estimations are performed using Bayesian statistical fits through a Python program employing the Markov Chain Monte Carlo method.

Taking into account the current tension of the Hubble constant between the observational values of the late universe and early universe [49], estimating the value of this constant by using new methods has great interest and is significantly important. The former measurements refer to local observations of Cepheids and Type Ia Supernovae, where astronomers use the luminosity-distance relation to obtain the Hubble constant $H_0 = 73.0 \pm 1.0$ km s^{-1} Mpc^{-1} [50]. The early universe measurements rely on Cosmic Microwave Background (CMB) observations. In this method, the astronomers analyze the temperature and polarization variations on the CMB with the ΛCDM model, statistically fitting the Hubble constant and obtaining the value $H_0 = 67.4 \pm 0.5$ km s^{-1} Mpc^{-1} [51]. Systematic errors have been considered in an effort to solve this tension. However, despite the increased precision in these measurements, the tension remains. In this work, we estimate the value of the late universe Hubble constant since we will be working with five black holes from galaxies located within the range of 30 Mpc - 150 Mpc from Earth.

In summary, the main goal of this thesis is to estimate the Hubble constant and the parameters of mass and distance of five black holes. By employing the SdS background, we incorporate the effects of dark energy with those caused by black holes, while avoiding the complexities introduced by matter in the universe. This general relativistic method offers an independent approach to obtain the Hubble constant, relying solely on redshift data of photons emitted from black hole accretion disks, rather than traditional distance indicators like Cepheids. This initial approach may be useful to analyze the relationship between black holes and cosmological properties, and it can be extended in future research to more realistic models that include matter and additional cosmological factors.

This thesis is organized as follows. Chapter 2 is dedicated to studying the SdS metric, examining the geodesic behavior of both massive and massless particles, as well as the redshift of photons as detected by a distant observer. Chapter 3 provides a brief review of the detection, data collection and mechanism of megamaser AGN systems, as well as their application in our modeling. In Chapter 4, we explain how to employ Bayesian statistics to estimate black hole parameters. We also implement the theoretical model with megamaser observations in a Python program to perform these estimations. Chapter 5 presents the results of the statistical estimations for the Hubble constant and black hole parameters of five galaxies. Finally, Chapter 6 discusses these results and presents the conclusions.

Chapter 2

Photon redshift in Schwarzschild-de Sitter spacetime

2.1 Schwarzschild-de Sitter metric

In this work, we consider the Einstein-Hilbert action with cosmological constant $\Lambda > 0$,

$$S = \int d^4x \sqrt{-g} \left(R - 2\Lambda \right), \tag{2.1}$$

where R is the Ricci scalar and g is the determinant of the metric tensor $g_{\mu\nu}$. By varying the action and using the least action principle, we obtain the Einstein field equations

$$R_{\mu\nu} - \frac{1}{2} R g_{\mu\nu} + \Lambda g_{\mu\nu} = 0, \tag{2.2}$$

where $R_{\mu\nu}$ is the Ricci tensor.

By solving the Einstein equations, we can obtain the SdS metric, which describes a spherically symmetric and static black hole in an expanding universe dominated by dark energy. This metric reads

$$ds^2 = -f dt^2 + f^{-1} dr^2 + r^2 d\Omega^2, \tag{2.3}$$

where $f = \left(1 - \frac{2M}{r} - \frac{\Lambda r^2}{3} \right)$ is the metric function in natural units, M is the black hole mass and $d\Omega^2 = d\theta^2 + \sin^2\theta d\phi^2$. The term $-2M/r$ corresponds to the gravitational potential of the black hole, and the term $-\Lambda r^2/3$ introduces the accelerated expansion of the universe.

In order to find the coordinate singularities of this metric, we need to solve the equation $f(r) = 0$. The three roots of the following cubic equation

$$\Lambda r^3 - 3r + 6M = 0 \tag{2.4}$$

follow the restriction $r_- < r_H < r_C$. Here, r_- represents a negative root and therefore has no physical meaning, while r_H and r_C are the event horizon radius and the cosmological horizon, respectively. The cosmological horizon is a one-way membrane such that even light cannot escape towards the observable universe and the null particles are purely outgoing at this radius. By fixing the cosmological constant, the values of r_H and r_C depend only on the mass; if M increases, the event horizon increases and the cosmological horizon decreases. In a similar manner, if we fix the mass and vary the cosmological constant, the event horizon increases as the cosmological constant increases, decreasing the cosmological horizon.

In this particular spacetime, there is another significant radius known as the zero-gravity radius (ZGR). At this radius, the gravitational pull of the black hole and the expansion of the universe cancel each other, creating a state of equilibrium. As a result, any static particle located at this radius remains static. A schematic illustration of the event horizon, the cosmological horizon and ZGR is shown in Figure 2.1.

2.2 Geodesic motion of a massive particle

Let us consider a massive particle with four-velocity $U^\mu = (U^t, U^r, U^\theta, U^\phi)$ in geodesic motion around a SdS black hole without perturbing its gravitational field.

The SdS metric has a temporal Killing vector $\xi^\mu = (1, 0, 0, 0)$ and an azimuthal Killing vector $\psi^\mu = (0, 0, 0, 1)$ related to the conserved quantities of energy E and the axial angular momentum L_ϕ, respectively, such that

$$U^\mu \xi_\mu = -E, \qquad U^\mu \psi_\mu = L_\phi. \tag{2.5}$$

Therefore, we can express the U^t and U^ϕ in terms of conserved quantities and metric components

$$U^t = -\frac{E}{g_{tt}}, \qquad U^\phi = \frac{L_\phi}{g_{\phi\phi}}. \tag{2.6}$$

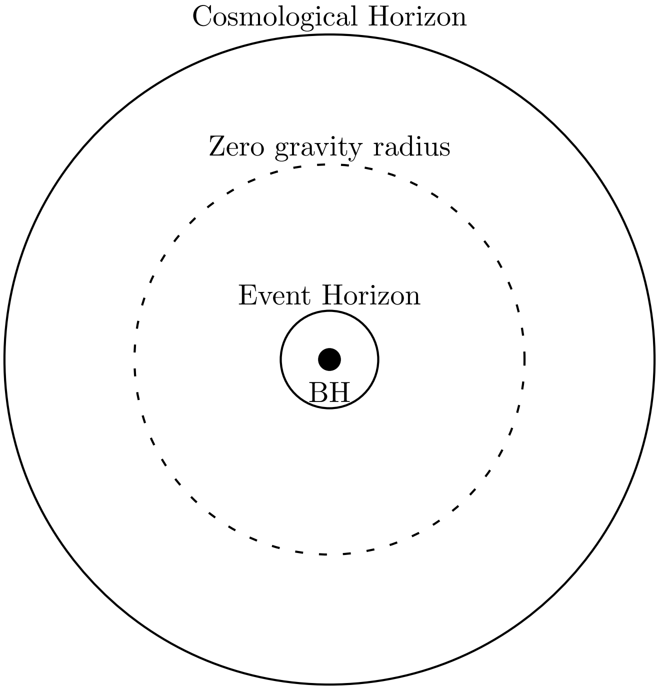

Figure 2.1: Schematic illustration of the cosmological horizon, zero gravity radius and event horizon of a SdS black hole.

We can insert these equalities in the four-velocity normalization $U^{\mu}U_{\mu} = -1$ to obtain

$$-1 = g_{rr}(U^r)^2 + g_{\theta\theta}(U^{\theta})^2 + \frac{E^2}{g_{tt}} + \frac{L_{\phi}^2}{g_{\phi\phi}}. \tag{2.7}$$

By rearranging terms and substituting the metric components, we can write the energy as

$$\frac{E^2}{2} = \frac{1}{2}(U^r)^2 + \frac{1}{2}\left(1 - \frac{2M}{r} - \frac{\Lambda r^2}{3}\right)\left(1 + r^2(U^{\theta})^2 + \frac{L_{\phi}^2}{r^2 \sin^2\theta}\right), \tag{2.8}$$

where we define an effective potential V_{eff} such that the total energy is given by $E_{tot} = E^2/2 = T + V_{eff}$, where $T = (U^r)^2/2$ is the kinetic energy and the effective potential is

$$V_{eff} = \frac{1}{2}\left(1 - \frac{2M}{r} - \frac{\Lambda r^2}{3}\right)\left(1 + r^2(U^{\theta})^2 + \frac{L_{\phi}^2}{r^2 \sin^2\theta}\right). \tag{2.9}$$

Now, we restrict the motion of the particle on the equatorial plane ($\theta = \pi/2$) and consider circular orbits. With these considerations, the four-velocity contains only two non-zero components $U^{\mu} = (U^t, 0, 0, U^{\phi})$, and the effective potential must satisfy the condition

$V'_{eff} = 0$[1]. In addition, we need the stability condition $V''_{eff} > 0$ to make sure it is a stable minimum.

By computing the derivative of the effective potential (2.9)

$$V'_{eff} = \frac{2L_\phi^2}{r^2}\left(\frac{3M}{r^2} - \frac{1}{r}\right) - 2\left(\frac{\Lambda r}{3} - \frac{M}{r^2}\right), \tag{2.10}$$

and equating to zero for circular orbits, we obtain the angular momentum

$$L_\phi = \pm r\sqrt{\frac{\frac{M}{r} - \frac{\Lambda r^2}{3}}{1 - \frac{3M}{r}}}, \tag{2.11}$$

Then, we substitute (2.11) in (2.8) to obtain an expression for the energy

$$E = \frac{1 - \frac{2M}{r} - \frac{\Lambda r^2}{3}}{\sqrt{1 - \frac{3M}{r}}}. \tag{2.12}$$

Finally, we insert E and L in (2.6) to get the four-velocity components for a massive test particle in circular geodesic motion ($U^r = 0$) restricted to the equatorial plane ($U^\theta = 0$), reading

$$U_e^t(r_e, \pi/2) = \frac{1}{\sqrt{1 - \frac{3M}{r_e}}}, \tag{2.13}$$

$$U_e^\phi(r_e, \pi/2) = \pm\frac{1}{r_e}\sqrt{\frac{\frac{M}{r_e} - \frac{\Lambda r_e^2}{3}}{1 - \frac{3M}{r_e}}}. \tag{2.14}$$

These four-velocity components are labeled with the subscript $_e$ and are evaluated at the emission point r_e, since we will assume this particle is a photon source.

2.3 Geodesic motion of a massless particle

The emitted photons of the test particle described in the previous section move in null geodesics with four-momentum $k^\mu = (k^t, k^r, k^\theta, k^\phi)$. Similarly to the massive particle

---

[1] Here $'$ denotes derivative with respect to the radial coordinate r

case, the conserved quantities associated to the Killing vectors are the energy E_γ and momentum L_γ

$$k^\mu \xi_\mu = -E_\gamma, \qquad k^\mu \psi_\mu = L_\gamma, \tag{2.15}$$

then, the time and the azimuthal components of the four-momentum can be expressed as

$$k_t = -E_\gamma, \qquad k_\phi = L_\gamma. \tag{2.16}$$

Since the motion of massless particles is confined to null geodesics, we have $k^\mu k_\mu = 0$. Considering relations (2.16), we have the equation

$$0 = g^{rr}(k_r)^2 + g^{\theta\theta}(k_\theta)^2 + g^{tt}(E_\gamma)^2 + g^{\phi\phi}(L_\gamma)^2. \tag{2.17}$$

In the previous section we assumed there is no motion on the polar coordinate θ, then $k_\theta = 0$, and we can write the radial component of the four-momentum as

$$\left(\frac{k_r}{E_\gamma}\right)^2 = \left(1 - \frac{2M}{r} - \frac{\Lambda r^2}{3}\right)^{-2} - \frac{L_\gamma^2}{E_\gamma^2 r^2}\left(1 - \frac{2M}{r} - \frac{\Lambda r^2}{3}\right)^{-1}. \tag{2.18}$$

We can define a parameter of interest that arises from the conserved quantities E_γ and L_γ: the light bending parameter or apparent impact factor $b = L_\gamma/E_\gamma$. In practice, it is hard to detect the frequency-shift of photons because of its small magnitude, so we focus on the points where the redshift is maximal. This occurs at the extremes of the orbit ($\phi \approx \pm\pi/2$) where the test particle, and therefore its emitted photons, have their maximum tangential velocity with respect to the observer, thus maximizing the chances of detecting the redshift/blueshift compared to the rest of the orbit. At these specific points, the photons move in the azimuthal direction towards the observer (see Figure 2.2), then $k_r = 0$, and the impact parameter at the edges of the disk is as follows

$$b_{e,\mp} = \mp \frac{r_e}{\sqrt{1 - \frac{2M}{r_e} - \frac{\Lambda r_e^2}{3}}}. \tag{2.19}$$

Since $b_\mp$ is defined as the quotient of two conserved quantities, it is also a conserved quantity along the whole path of the photons from emission to detection. Nevertheless, note that this expression is calculated for emission at the extremes of the disk[2].

---

[2] The test particle emits photons at all points of the orbit and they all could arrive to the distant observer. We consider the photons emitted at the extremes of the disk, because the redshift at these points maximizes, as explained in the previous paragraph. Expression (2.19) is calculated for these extreme points.

Now, we can rewrite equation (2.18) in terms of this impact parameter as follows

$$\left(\frac{k_r}{E_\gamma}\right)^2 = \left(1 - \frac{2M}{r} - \frac{\Lambda r^2}{3}\right)^{-2} - \frac{b_{e,\mp}}{r^2}\left(1 - \frac{2M}{r} - \frac{\Lambda r^2}{3}\right)^{-1}. \tag{2.20}$$

2.4 Geodesic motion of a far away observer

In the previous sections, we obtained the four-velocity of a test particle circularly orbiting the black hole, along with the four-momentum of its emitted photons. Now, we consider another test particle located far away from the SdS black hole which detects the emitted photons. In the Schwarzschild metric, for $r \to \infty$, the observer can be considered at rest with respect to the black hole, with its four-velocity $U^\mu_{Schw} = (1, 0, 0, 0)$. Nevertheless, the SdS metric is not asymptotically flat but asymptotically de Sitter. Therefore, the effect of the cosmological constant dominates for large distances and the massive particle moves away from the black hole due to the accelerated expansion of the universe, created by the cosmological constant. Then, the radial velocity of the test particle is non-zero and recedes from the black hole.

Considering the particle is not moving in the polar and azimuthal directions, we set $U^\theta = 0$ and $L_\phi = 0$, and use (2.8) to determine U^r as follows

$$(U^r)^2 = -\left(1 - \frac{2M}{r} - \frac{\Lambda r^2}{3}\right) + E^2. \tag{2.21}$$

In order to find the energy expression, we use the conservation of energy law and the ZGR. As stated in Section 2.1, the ZGR indicates the radius at which a particle remains at rest because of the cancellation between the gravitational potential of the black hole and that of the expansion of the universe. Its angular momentum is given by (2.11) and vanishes since there is no motion in the azimuthal direction, then,

$$L_\phi = r_{zg}\sqrt{\frac{\dfrac{M}{r_{zg}} - \dfrac{\Lambda r_{zg}^2}{3}}{1 - \dfrac{3M}{r_{zg}}}} = 0, \tag{2.22}$$

hence, the ZGR is given by

$$r_{zg} = \left(\frac{3M}{\Lambda}\right)^{1/3}. \tag{2.23}$$

By setting $U^r = 0$ in equation (2.21) and substituting the ZGR we can see that the energy reads

$$E = \sqrt{1 - (3M)^{2/3}\Lambda^{1/3}}. \tag{2.24}$$

Because of the energy conservation, this is not only the energy for this radius, but also for greater radii than the ZGR.

Finally, we can use this energy in the first equality of (2.6) and in (2.21) to obtain the four-velocity components of a far away observer with receding radial motion from the black hole

$$U_d^t(r_d) = \frac{\sqrt{1-(3M)^{2/3}\Lambda^{1/3}}}{1-\dfrac{2M}{r_d}-\dfrac{\Lambda r_d^2}{3}}, \tag{2.25}$$

$$U_d^r(r_d) = \sqrt{\frac{2M}{r_d}+\frac{\Lambda r_d^2}{3}-(3M)^{2/3}\Lambda^{1/3}}. \tag{2.26}$$

Here, the subscript $_d$ indicates that these four-velocities are valid for the detector at r_d.

In Figure 2.2 a schematic view of the SdS black hole is presented, illustrating the orbiting photon source and a distant observer.

2.5 Redshift

Determining the frequency shift of photons is important, as it is a commonly measured quantity in astrophysical observations through high-resolution spectrometry. Additionally, the shift in the frequency is an invariant quantity, meaning it does not depend on the reference frame in which it is measured. Hence, in this section we are going to find an expression for the redshift in terms of the metric variables.

The redshift (z_1) or blueshift (z_2) of a photon is defined as the relative change between its detected wavelength and its emitted wavelength. This relationship can be expressed mathematically as

$$z_{1,2} = \frac{\lambda_d - \lambda_e}{\lambda_e}. \tag{2.27}$$

Here the subscripts $_d$ and $_e$ indicate the detection point and emission point, respectively. In terms of frequency, we can write

$$1 + z_{1,2} = \frac{\omega_e}{\omega_d}, \tag{2.28}$$

where ω_i is the photon frequency at either point of emission or detection.

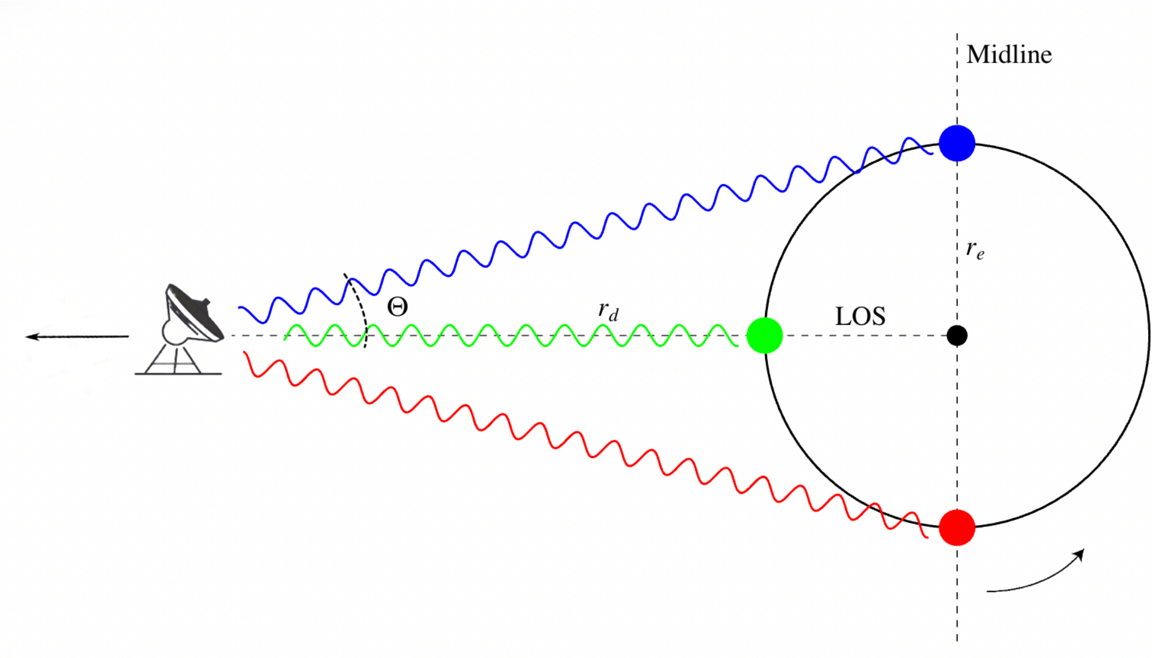

Figure 2.2: A photon source at r_e circularly orbiting the SdS black hole and an observer at a distance r_d, which is receding from the black hole system. The observer measures the frequency shift and the position on the sky Θ of the photon source. At the edges of the disk, the test particle has its maximum tangential velocity, leading to the detection of redshift/blueshift of the emitted photons. The midline connects the disk's edges with the central black hole, while the line of sight (LOS) connects the observer to the black hole.

Using natural units ($\hbar = 1$), the energy of a photon is given by $E_\gamma = \omega$. Therefore, the frequency of a photon measured by an observer with four-velocity U^μ is given by

$$\omega = -k_\mu U^\mu. \tag{2.29}$$

Then, the frequency shift of emitted photons in the vicinity of a SdS black hole and detected by an observer on the Earth reads

$$1 + Z_{SdS_{1,2}} = \frac{\left(-k_t U^t - k_\phi U^\phi\right)_e}{\left(-k_t U^t - k_r U^r\right)_d}. \tag{2.30}$$

After substituting the four-momentum (2.16) and dividing by E_γ, Eq. (2.30) converts to

$$1 + Z_{SdS_{1,2}} = \frac{\left(U^t - b_\mp U^\phi\right)_e}{\left(U^t - \frac{k_r}{E_\gamma} U^r\right)_d}, \tag{2.31}$$

where $b_{\mp}$ is the impact parameter defined in equation (2.19). Now, we can substitute the four-velocity components for the emission point (2.13)-(2.14) and the detection point (2.25)-(2.26), as well as the term k_r/E_γ from (2.20) into relation (2.31). The resulting full expression of the redshift reads

$$1 + Z_{SdS_{1,2}} = \frac{1}{\sqrt{1-3\tilde{M}}} \times \frac{\left(1 \pm \sqrt{\dfrac{\tilde{M}-\tilde{\Lambda}}{1-2\tilde{M}-\tilde{\Lambda}}}\right)\left(1-2\bar{M}-\bar{\Lambda}\right)}{\sqrt{1-(3M)^{2/3}\Lambda^{1/3}} - \sqrt{2\bar{M}+\bar{\Lambda}-(3M)^{2/3}\Lambda^{1/3}}\sqrt{1-\left(\dfrac{r_e}{r_d}\right)^2 \dfrac{1-2\bar{M}-\bar{\Lambda}}{1-2\tilde{M}-\tilde{\Lambda}}}}. \tag{2.32}$$

where we redefined the variables as $\tilde{M} = M/r_e$, $\tilde{\Lambda} = \Lambda r_e^2/3$, $\bar{M} = M/r_d$ and $\bar{\Lambda} = \Lambda r_d^2/3$.

We can express the redshift as the sum of the gravitational redshift Z_g and the kinematic redshift $Z_{kin1,2}$ such that

$$Z_{SdS_{1,2}} = Z_g + Z_{kin_{1,2}}. \tag{2.33}$$

The gravitational redshift can be distinguished from the kinematic redshift since it arises from the curvature of spacetime caused by the black hole mass and the cosmological constant, and does not depend on the particle's motion around the black hole. Therefore, only the time component of the emitter's four-velocity will give rise to the gravitational redshift. Based on this understanding, from (2.31), we obtain an expression for Z_g

$$1 + Z_g = \frac{1}{\sqrt{1-3\tilde{M}}} \times \frac{1-2\bar{M}-\bar{\Lambda}}{\sqrt{1-(3M)^{2/3}\Lambda^{1/3}} - \sqrt{2\bar{M}+\bar{\Lambda}-(3M)^{2/3}\Lambda^{1/3}}\sqrt{1-\left(\dfrac{r_e}{r_d}\right)^2 \dfrac{1-2\bar{M}-\bar{\Lambda}}{1-2\tilde{M}-\tilde{\Lambda}}}}. \tag{2.34}$$

On the other hand, since the kinematic redshift arises from the particle's motion around the black hole, the azimuthal component of the emitter's four-velocity generates this redshift, reading

$$Z_{kin_{1,2}} = \pm \frac{\sqrt{\tilde{M}-\tilde{\Lambda}}}{\sqrt{1-3\tilde{M}}\sqrt{1-2\tilde{M}-\tilde{\Lambda}}} \times \frac{1-2\bar{M}-\bar{\Lambda}}{\sqrt{1-(3M)^{2/3}\Lambda^{1/3}} - \sqrt{2\bar{M}+\bar{\Lambda}-(3M)^{2/3}\Lambda^{1/3}}\sqrt{1-\left(\dfrac{r_e}{r_d}\right)^2 \dfrac{1-2\bar{M}-\bar{\Lambda}}{1-2\tilde{M}-\tilde{\Lambda}}}} \tag{2.35}$$

Note that the expansion of the universe contributes to both redshifts through the cosmological constant.

Furthermore, we can compose the SdS redshift (2.32) with a relativistic boost to consider the redshift due to the peculiar motion of the system. This composition is presented in Appendix 1.

2.5.1 Redshift approximation

Hereinafter we consider megamaser systems for our model. In these systems, the photon source is a water vapor cloud located in the accretion disk at $r_e < 1\text{pc}$ from a supermassive black hole with mass $M \sim 10^6\ \mathrm{M}_\odot$, at a distance $r_d > 30$ Mpc from the Earth, this lower bound of the distance is chosen in order to consider photon sources located within the Hubble flow. Considering this configuration, and the fact that the cosmological constant is of the order of $\Lambda \sim 10^{-52}\ \mathrm{m}^{-2}$, we have the following constraints

$$\frac{M}{r_e} > 10^{-6}, \qquad \Lambda r_d^2 > 10^{-6},$$

$$\frac{M}{r_d} < 10^{-13}, \qquad \Lambda r_e^2 < 10^{-20}.$$

By expanding equation (2.32) for $M/r_d \to 0$, $\Lambda r_e^2 \to 0$ and $\Lambda r_d^2 \to 0$, and keeping the first dominant term in Λr_d^2, the SdS redshift can be expressed as the following product [36]

$$1 + Z_{SdS_{1,2}} = (1 + Z_{Schw_{1,2}})(1 + Z_\Lambda), \tag{2.36}$$

where $Z_{Schw1,2}$ corresponds to the frequency shift in the Schwarzschild spacetime [45]

$$1 + Z_{Schw_{1,2}} = \sqrt{\frac{1}{1-3\tilde{M}}} \pm \sqrt{\frac{\tilde{M}}{(1-3\tilde{M})(1-2\tilde{M})}}, \tag{2.37}$$

which we can also express as a sum of gravitational and kinematic redshifts in a simmilar manner to the SdS case (2.33)

$$Z_{Schw_{1,2}} = Z_{g,Schw} + Z_{kin_{1,2},Schw}, \tag{2.38}$$

where the gravitational and kinematic redshifts for this case read

$$1 + Z_{g,Schw} = \sqrt{\frac{1}{1-3\tilde{M}}}, \tag{2.39}$$

$$Z_{kin_{1,2},Schw} = \pm\sqrt{\frac{\tilde{M}}{(1-3\tilde{M})(1-2\tilde{M})}}. \tag{2.40}$$

On the other hand, he cosmological redshift Z_Λ reads

$$1 + Z_\Lambda = 1 + \sqrt{\frac{\Lambda}{3}}r_d = 1 + H_0 r_d, \tag{2.41}$$

where we used the relation

$$H_0 = \sqrt{\frac{\Lambda}{3}}. \tag{2.42}$$

Using this relation introduces a model-dependency in our results, as it derives from the standard model of cosmology, when neglecting the matter content of the universe, since the SdS background accounts solely for dark energy. Note that Equation (2.41) is the Hubble law.

Thus, we have a formula for the frequency shift, which is a directly measurable quantity, in terms of the metric parameters and the Hubble constant.

Chapter 3

Megamaser AGN systems

3.1 Astrophysical megamasers

Astrophysical masers (Microwave Amplification by Stimulated Emission of Radiation) consist of high-density gas clouds that emit radiation in the microwave regime. This emission occurs when an external energy source induces a population inversion in the gas, meaning there are more particles in an excited energy state than in a low state. When microwave photons interact with these excited particles, stimulated emission occurs, leading to the amplification of the microwave radiation.

H_2O megamasers emit at the 22 GHz transition line of water molecules and are extremely luminous $L > 100L_\odot$ (10^6 times brighter than galactic masers). Very Long Baseline Interferometry (VLBI) has been widely used look for these water vapor systems by observing at 22 GHz. Moreover, VLBI provides the submilliarcsecond resolution needed to map the sub-parsec maser disks [41]. Most of these water megamaser systems arise in high-density circumnuclear disks with an AGN as the energy source for the stimulated emission [52]. In particular, they are found on accretion disks orbiting a central mass of the order $10^6 - 10^7\mathrm{M}_\odot$ at sub-parsec radii [40].

Megamaser disks are observed edge-on, with three groups of maser features observed on the sky: the masers on the extremes of the disk (which exhibit redshift and blueshift due to the rotation of the disk), and the central maser features [39], as illustrated in Figure 3.1. Henceforth, the former two maser groups will be called highly frequency-shifted masers, and the masers located along the line of sight (LOS; the line that connects the observer to the black hole) will be referred to as systemic masers. This configuration

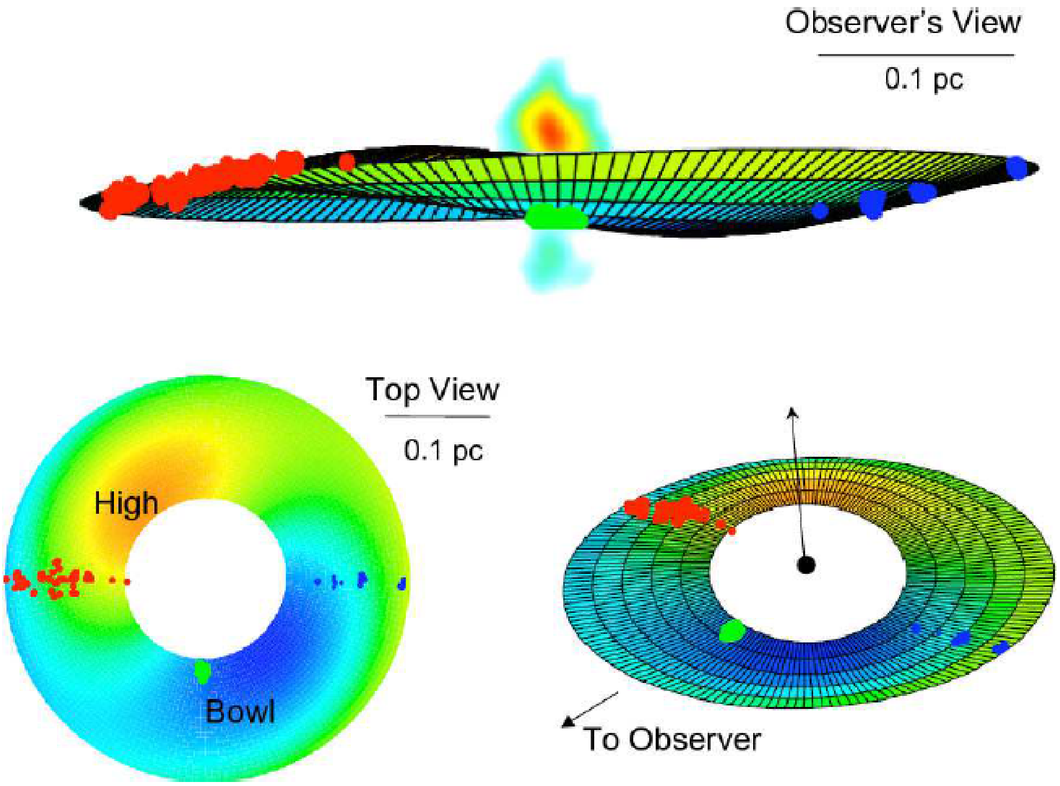

Figure 3.1: H_2O megamaser features configuration. There are three groups of megamasers observed edge-on on the sky. The figure is taken from [56].

arises because, at the edges of the disk, the velocity gain paths are the longest, providing the necessary conditions for amplifying radiation due to velocity coherence along these paths. The systemic masers originate because the central energy engine stimulates the vapor clouds located along the LOS, producing the emission of coherent light directly towards the observer.

The megamaser system at the core of NGC 4258, discovered in 1984, has been thoroughly studied and has significantly contributed to the modeling of megamaser systems [53, 54, 55]. Ever since its discovery, numerous observations have been conducted, making it the most studied megamaser system and achieving a great number of data. It represents the archetypal model for water megamaser configurations, exhibiting a thin annular disk viewed edge-on, as shown in Figure 3.1.

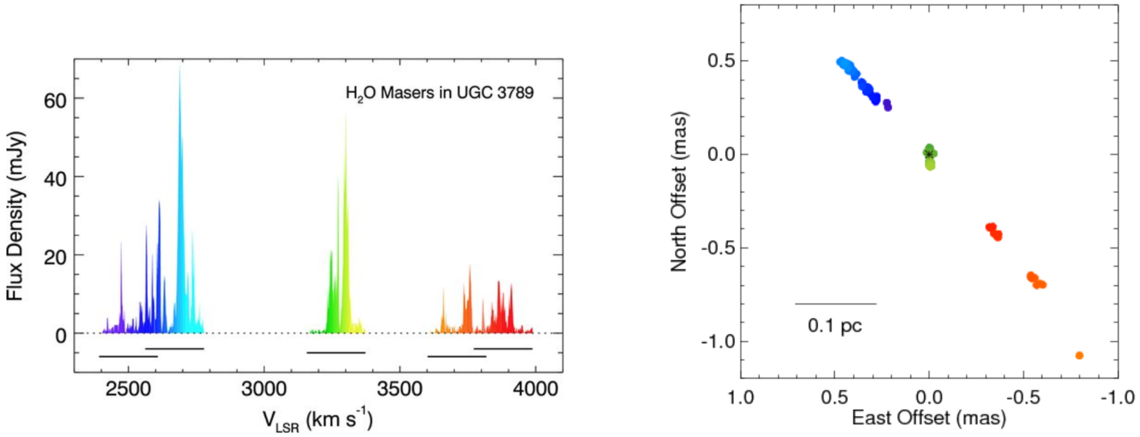

Figure 3.2: MCP measurements of UGC 3789 as reported in [57]. The left figure shows the measured redshift in terms of velocity using the optic definition of the redshift $v = cz$. The right figure displays the sky position of the masers.

3.2 Megamaser observation and data

Throughout the years, surveys of thousands of AGNs have been conducted to identify megamaser AGNs, and around a hundred of such systems have been identified. These astrophysical observations have been carried out using Very Long Baseline Interferometry (VLBI) since this technique provides the submilliarcsecond resolution needed to map the sub-parsec maser disks [41].

The Megamaser Cosmology Project (MCP)[1] is a National Radio Astronomy Observatory (NRAO) key project that aims to measure the Hubble constant using megamaser AGNs located within the Hubble flow[2]. The MCP conducts surveys to find megamaser AGNs and maps the maser features found in each galaxy, measuring the following quantities for each maser feature

- Frequency shift z_{obs}.

- Position on the sky (x, y) measured in milliarcseconds (mas). This is the aperture angle of the telescope when observing the positions on the sky of the masers.

---

[1] More information in: `https://safe.nrao.edu/wiki/bin/view/Main/MegamaserCosmologyProject`

[2] The Hubble flow describes the receding motion of the galaxies due solely to the expansion of the Universe. This effect becomes more pronounced at distances greater than 30 Mpc.

- Error in positions (σ_x, σ_y).
- Acceleration of the masers and error in the acceleration.

These measurements are illustrated in Figure 3.2 for the UCG 3789 galaxy reported in [57], where the three groups of maser features (the highly frequency-shifted and the systemic) are visible. This project has mapped over 20 megamaser galaxies (e.g., [42, 43, 44]) using VLBI techniques with the Very Large Baseline Array (VLBA), the Radio Telescope Effelsberg (ET), the Robert C. Byrd Green Bank Telescope (GBT) and the Karl G. Jansky Very Large Array (VLA).

In [47] and [48], 14 of these megamaser AGN systems are studied using a general relativistic model (considering a Schwarzschild black hole), statistically fitting the black hole parameters by means of the MCP data. Out of these 14 galaxies, 12 are located within the Hubble flow, namely NGC 1194, NGC 1320, NGC 2960, UGC 3789, NGC 5495, NGC 5765b, NGC 6264, NGC 6323, Mrk 1029, CGCG 074-064, ESO 558-G009 and J0437+2456. In this work, we are interested in statistically estimating the Hubble constant, so we mainly focus on the ones that are farther away into the Hubble flow, as well as the ones that have the highest number of data and the highest precision.

In summary, we use the MCP data of frequency shift and sky positions of the maser features, along with their corresponding errors, as reported in [33, 42, 43, 58, 59, 60, 61] for the 12 aforementioned galaxies. Our primary focus is on the galaxies UGC 3789, NGC 5765b, NGC 6264, NGC 6323 and CGCG 074-064 because of the previously mentioned criteria (the images of the host galaxies are presented in Figure 3.3).

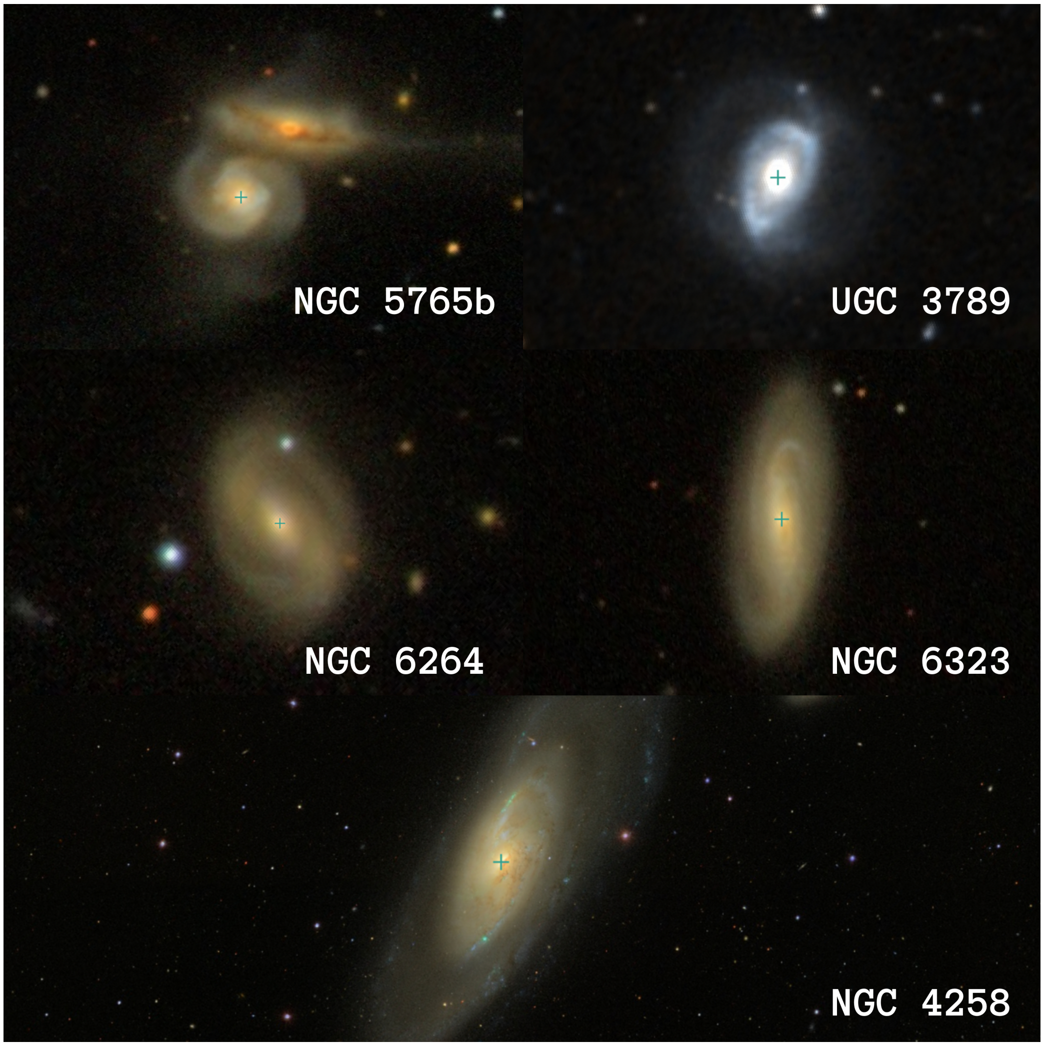

Figure 3.3: Megamaser host galaxies. The images are taken from the Aladin sky atlas.

Chapter 4

Bayesian statistical fit

4.1 Bayesian statistics

In this thesis, we aim to estimate black hole parameters and the Hubble constant. We achieve these estimations using Bayesian inference, a method widely employed in cosmology for parameter fitting when having large datasets [62].

Unlike the frequentist approach to statistics, Bayesian statistics incorporates the prior knowledge of an event into the calculation of the posterior probability of said event. Mathematically, this is expressed by the Bayes' theorem

$$p(m|d) = \frac{p(m)p(d|m)}{p(d)}, \tag{4.1}$$

where $p(m|d)$ represents the posterior probability that the model m is true given the data d, $p(m)$ is the prior probability of the model, $p(d)$ is the probability of the data occurring under all possible models, and $p(d|m)$ is called the likelihood, which is the probability of obtaining the data with the given the model.

In other words, the posterior probability of a certain hypothesis or model is proportional to its prior probability and the likelihood [63],

$$\textit{posterior} \propto \textit{prior} \times \textit{likelihood}. \tag{4.2}$$

These quantities have an associated probability density function (PDF). We can write the PDF of the likelihood $\mathcal{L}$ of a parameter x as follows

$$\mathcal{L}(x) = \frac{1}{\sqrt{2\pi\sigma^2}} \exp\left[-\frac{1}{2\sigma^2}(x-\mu)^2\right]. \tag{4.3}$$

This represents a Gaussian distribution, where the mean value is μ with some error σ. The term multiplying the exponential is a normalising constant. Given that the likelihood is related to the probability of obtaining the data given a model, the mean μ is the value of a measurement and the error σ is the associated uncertainty of the measurement.

The prior PDF is usually represented as a flat or a Gaussian distribution, depending on the previously provided information. The shape of the posterior PDF, on the other hand, is influenced by the prior PDF and the likelihood PDF. It is desired that the PDF of the posterior takes the form of a Gaussian, with a most-probable value x_0 and some error σ_0. This posterior value with its error is the result of the parameter estimation.

4.1.1 Goodness of fit

The goodness of fit indicates how well a dataset matches the values predicted by a theory. One common measure of goodness of fit is the reduced Pearson's χ^2, which relates to the likelihood as follows

$$\ln \mathcal{L} \propto -\frac{\chi^2}{2} \tag{4.4}$$

Explicitly writing the reduced Pearson's χ^2, we have

$$\frac{\chi^2}{N} = \sum_{i}^{N} \frac{(data_i - model)^2}{\sigma_i^2} \tag{4.5}$$

where σ_i is the error of the i-th data point, and N is the number of observational data [64].

To increase the goodness of fit of the model means increasing the probability of obtaining the experimental data given the theoretical model. For this, we have to maximize the likelihood (4.3), and therefore minimize the reduced Pearson's χ^2. The more the reduced Pearson's χ^2 approaches to unity, the more likely it is that our general relativistic model fits the astrophysical data.

4.2 Implementing the model on megamaser redshift observations

As stated in Section 3.2, we use megamaser astrophysical data to fit our model and determine the black hole parameters of mass M, position on the sky (x_0, y_0), distance r_d and the Hubble constant H_0. The astrophysical observations consist of the redshift z_{obs}, positions on the sky (x, y) and position uncertainties (σ_x, σ_y) of the maser features. The position measurements are actually aperture angles Θ of the telescope, while in our model we need the radius of the emitter r_e. We can express the emitter radius in terms of the aperture angle and the distance from the Earth to the black hole for the highly frequency-shifted masers by making the approximation $r_e \approx r_d\Theta$ (see Figure 2.2 for more clarity), with $\Theta^2 = (x - x_0)^2 + (y - y_0)^2$. In this way, we can explicitly write the redshift in terms of the black hole mass, its distance to Earth, the sky position of the photon source and the Hubble constant, (i. e. in terms of the black hole parameters and the observed quantities).

For simplicity and clarity, we write the explicit expression for the approximated redshift (2.36) instead of equation (2.32), given that it is lengthy (see Appendix 2 for the full expressions),

$$1 + Z_{SdS_{1,2}} = \left(\sqrt{\frac{1}{1 - 3\dfrac{M}{r_d\Theta}}} \pm \sqrt{\frac{\dfrac{M}{r_d\Theta}}{\left(1 - 3\dfrac{M}{r_d\Theta}\right)\left(1 - 2\dfrac{M}{r_d\Theta}\right)}} \right) (1 + H_0 r_d) \,. \tag{4.6}$$

Now, using the goodness of fit (4.5), we can test this general relativistic model against the astrophysical observations of megamasers' redshift. Employing expression (2.36) of the redshift, we obtain the following χ^2/N

$$\frac{\chi^2}{N} = \sum_{i=1}^{N} \frac{\left[Z_{obs,i} - (1 + Z_{grav} + \varepsilon \sin\theta_0 Z_{kin_{1,2}})(Z_\Lambda + 1) + 1\right]^2}{\delta Z_{SdS}^2 + \left(\beta Z_{kin_{1,2}}(1 + Z_\Lambda)\right)^2}, \tag{4.7}$$

where $Z_{obs,i}$ is the observed redshift of the i-th maser spot and δZ_{SdS} is its observational uncertainty. We have also introduced the correcting factors $\sin\theta_0$, ε and β. The former factor considers small deviations of the disk from the equatorial plane ($\theta_0 \sim \pi/2$). The other two factors account for deviations of masers about the midline, meaning the masers are spread by a small angle $\delta\phi$ on the midline ($\phi = \pi/2 \pm \delta\phi$)

$$\varepsilon \approx 1 - \frac{\delta\phi^2}{2} + \frac{\delta\phi^4}{24}, \qquad\qquad \beta \approx \frac{\delta\phi^2}{2}, \tag{4.8}$$

where ε corresponds to the expansion of the cosine function for small angles, and β is the variation of this expansion.

We can write the observational uncertainty of the SdS redshift (4.6) as the variation

$$\delta Z_{SdS} = (\delta Z_{grav} \pm \varepsilon \sin\theta_0 \delta Z_{kin})(1 + Z_\Lambda), \tag{4.9}$$

where the errors of the gravitational redshift δZ_{grav} and the kinematic redshift δZ_{kin} are [45]

$$\delta Z_{grav} = -\frac{3}{2}(1+Z_{grav})^3 \frac{M}{r_d\Theta}\left(\frac{\delta\Theta}{\Theta}\right), \tag{4.10}$$

$$\delta Z_{kin} = \frac{1}{2}Z^3_{kin\pm}\frac{r_d\Theta}{M}\left(\frac{6M^2}{(r_d\Theta)^2}-1\right)\left(\frac{\delta\Theta}{\Theta}\right). \tag{4.11}$$

Finally, $\delta\Theta$ is related to the uncertainty of the measured position, reading

$$\delta\Theta = \sqrt{\left(\frac{x-x_0}{\Theta}\right)^2\sigma_x^2 + \left(\frac{y-y_0}{\Theta}\right)^2\sigma_y^2}. \tag{4.12}$$

Note that in every expression involving the redshift (i.e equations (4.6), (4.10) and(4.11)), the mass and the distance are always in the form $\frac{M}{r_d}$, while the Hubble constant and the distance are also coupled as $H_0 r_d$. Because of this coupling, it is not possible to independently estimate M, r_d and H_0, but the quantities M/r_d and $H_0 r_d$.

4.3 Statistical fit via Python

To perform the statistical estimations, we use a Python program that employs the Markov Chain Monte Carlo (MCMC) method, which is widely used in Bayesian inference because of its power to explore high-dimensional parameter spaces.

This computational method consists of generating a series of random samples for the parameter to be estimated, known as Markov chains. Each sample value is assigned a probability based on the given prior and the likelihood, looking for minimizing the reduced Pearson's χ^2 (4.5). This set of sample values forms a posterior probability distribution, from which the most probable value is taken as the posterior estimate, along with an associated error. The more number of chains, the more the posterior probability distribution is defined, leading to a better posterior estimation [65].

In this way, we input the reduced Pearson's χ^2 corresponding to our model (B.2) in the Python program with $\sim 10^5 - 10^6$ chains to fit the following parameters of each of the five galaxies (UGC 3789, NGC 5765b, NGC 6264, NGC 6323 and CGCG 074-064)

- Mass-to-distance ratio of the black hole M/r_d.
- Position of the black hole (x_0, y_0).
- The Hubble constant times the distance $H_0 r_d$.

We perform the Bayesian statistical fit for each galaxy individually as well as for all the five galaxies together. By performing the estimations with the five galaxies combined, we correlate them through the H_0 value, which is a common variable present in all of the five galaxies. Also, for this particular estimation we use a Gaussian prior for the Hubble constant to decouple the quantities M/r_d and $H_0 r_d$ to estimate M, r_d and H_0 independently.

Given the large number of parameters to be estimated and a great number of observational data for all the galaxies, a high number of chains is required to obtain reliable estimations, making the process computationally expensive. Therefore, we use IFUAP's cluster and the Cuetlaxcoapan cluster from the Laboratorio Nacional de Supercómputo del Sureste de México to execute the Python program, taking advantage of their high computational performance. In the next Chapter, the results of these estimations are presented.

Chapter 5

Results

From the twelve galaxies mentioned in Chapter 3, we focus on individual estimations for the five galaxies with the greatest number of data and best precision. These galaxies are UGC 3789, NGC 5765b, NGC 6264, NGC 6323 and CGCG 074-064. Additionally, we perform a combined statistical fit using the data from these five galaxies, since it is advantageous to combine the datasets to obtain a more accurate value of the Hubble constant. By correlating the data from these galaxies within a single program, we enhance the precision of our results.

As mentioned in the previous Chapter, we use a Bayesian statistical fit that minimizes the reduced Pearson's χ^2 (B.2) using the observational data and relating it to our theoretical model (B.1). The data sources for each galaxy are displayed in Table 5.1, from where we also recover the inclination angles θ_0.

System	θ_0 ($^\circ$)	Source
UGC 3789	90.6	Reid et al. (2013) [33]
NGC 5765b	94.5	Gao et al. (2015) [60]
NGC 6264	89.5	Kuo et al. (2012) [58]
NGC 6323	88.5	Kuo et al. (2014) [59]
CGCG 074-064	90.8	Pesce et al. (2020) [61]

Table 5.1: Data sources for each galaxy and their corresponding inclination angles recovered from these references.

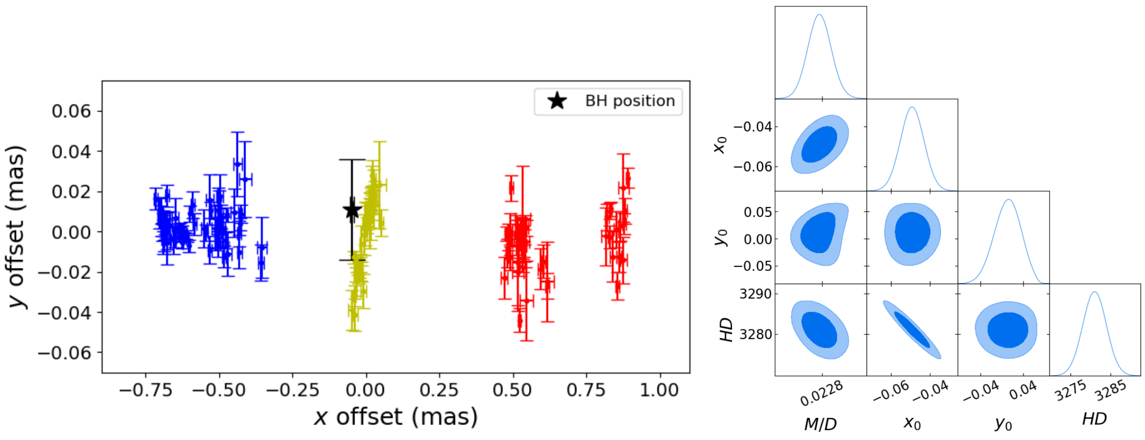

Figure 5.1: Maser features in the sky, black hole posterior position and posterior probability distributions for UGC 3789.

5.1 Estimation of individual galaxies

The parameters that undergo a Bayesian statistical fit are the mass-to-distance ratio M/r_d, the product H_0r_d and the position $(x_0, y_0)^1$. For each system we fixed the scattering angle of maser features $\delta\phi$ such that the reduced χ^2 reaches a value close to unity. The posterior fitting results are summarized in Table 5.2. In Figures 5.1-5.5, the posterior probability distributions of the parameters and their confidence regions for every system are shown, as well as images of the maser features in the sky with their corresponding error and the estimated black hole position (x_0, y_0) on the sky with its errors.

5.1.1 UGC 3789

Although this maser disk is thin, it is possible to estimate the black hole position on the y axis. The posterior position of this galaxy resulted to be near the geometric center, slightly off the systemic masers. The maser features are scattered about the midline with an angle of $\delta\phi = 10°$, and the best reduced χ^2 fit is 1.40.

5.1.2 NGC 5765b

For this galaxy, we find the scattering of the masers about the midline to be $\delta\phi = 10°$, and we obtain a reduced χ^2 of 1.15. Since the disk of this galaxy has an inclination

---

[1] For NGC 6264 the position y_0 could not be estimated, and therefore was fixed.

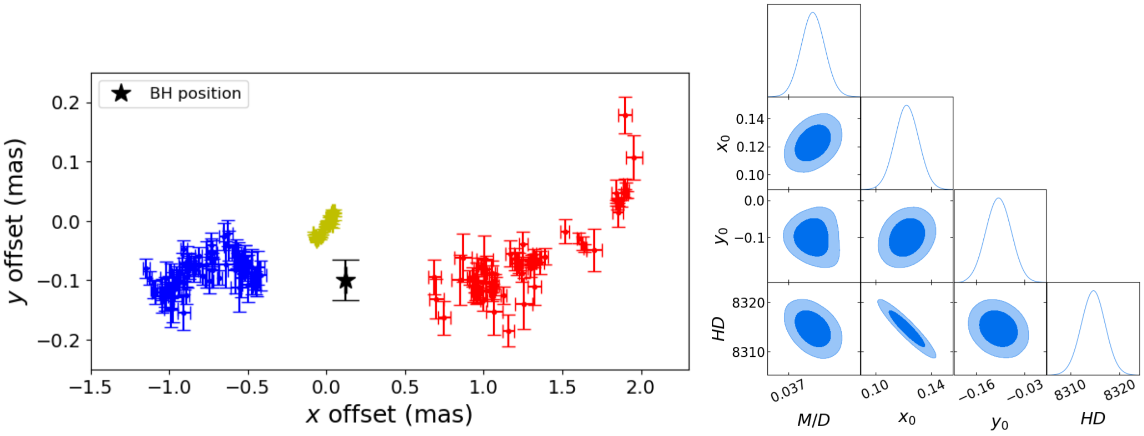

Figure 5.2: Maser features in the sky, black hole posterior position in the sky, and posterior probability distributions for NGC 5765b.

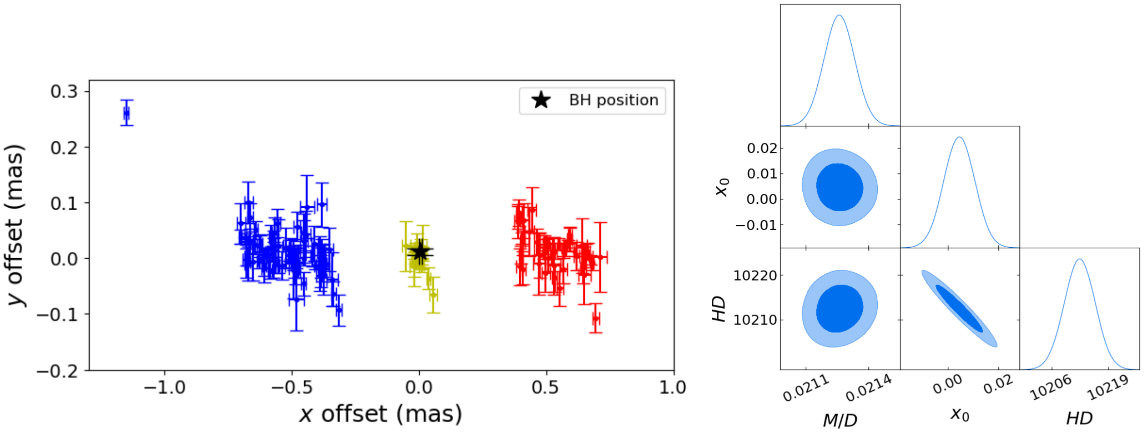

Figure 5.3: Maser features in the sky, black hole posterior position in the sky, and posterior probability distributions for NGC 6264.

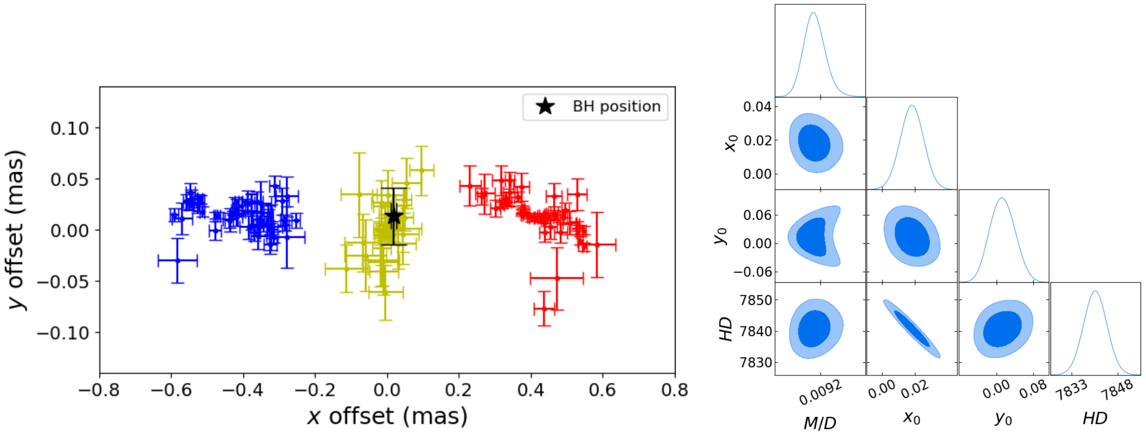

Figure 5.4: Maser features in the sky, black hole posterior position in the sky, and posterior probability distributions for NGC 6323.

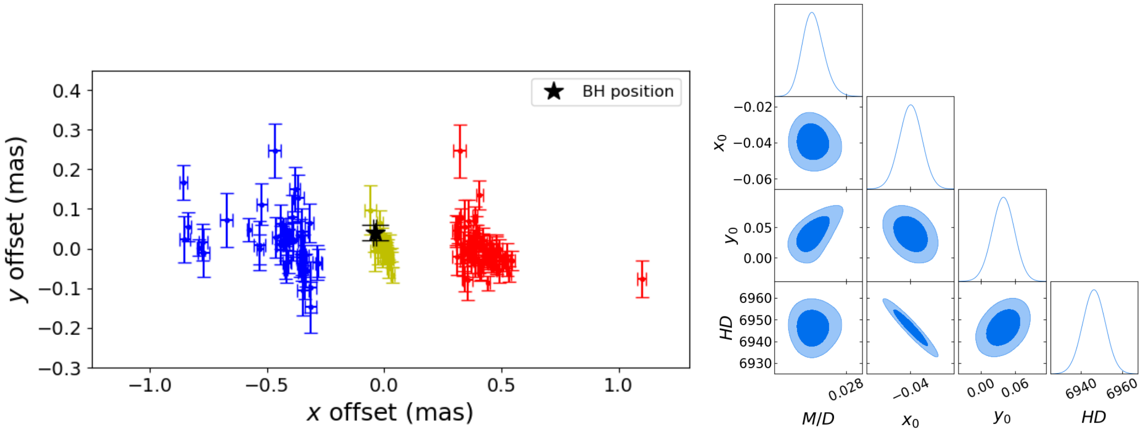

Figure 5.5: Maser features in the sky, black hole posterior position in the sky, and posterior probability distributions for CGCG 074-064.

angle of $\theta_0 = 94.5°$ [60], the LOS masers seem misaligned with the redshifted and blueshifted masers. Besides, more redshifted maser features are observed in a wider y offset range in comparison to the blueshifted ones. As a result of the Bayesian statistical fit, we find the black hole position to be near the geometric center formed by the redshifted and the blueshifted maser features.

5.1.3 NGC 6264

For this galaxy in particular, we perform the Bayesian statistical fit for three parameters, fixing y_0 at the geometric center of the disk formed by the highly frequency-shifted masers at a y offset of 0.030 mas [47]. We vary the y_0 offset along the height of the disk and find variations on M/r_d of less than 0.012%, which is inside the error. The angle on which the highly frequency-shifted masers are spread about the midline is $\delta\phi = 10°$, rendering a reduced $\chi^2 = 1.28$. In Figure 5.3 the error on the y offset is not shown because the y_0 position is fixed. Furthermore, since we vary the y_0 offset along the height of the disk and find negligible variations on the results, we can assert the y_0 offset may be in any position along the height of the disk.

5.1.4 NGC 6323

The three groups of maser features in this galaxy are almost aligned with each other, with an inclination angle of nearly 90° [59]. The reduced χ^2 we find is 1.26, and the scatter angle is $\delta\phi = 11°$. Although in this galaxy the error on the x offset is bigger than in the rest of the galaxies, the error on the estimated black hole x offset does not increase significantly, as seen in Figure 5.3.

5.1.5 CGCG 074-064

For this system, the observed maser features seem aligned with each other, and the disk practically edge on, with an inclination angle of 90.8° [61]. The posterior position of the black hole is near the geometric center, behind the systemic masers. For this galaxy, we obtain a reduced $\chi^2 = 1.27$ with a scattering angle of $\delta\phi = 11°$. Note, in Figure 5.5, that the error in the posterior y_0 offset seems significantly smaller compared to the rest of the galaxies. Actually, the errors on the y offset of the maser features of this dataset are greater than the errors in the rest of the galaxies, so it could be expected to have a larger

System	M/r_d ($10^5 M_\odot$/Mpc)	$H_0 r_d$ (km/s)	x_0 (mas)	y_0 (mas)	$\delta\phi$ (°)	χ^2_{red}
UGC 3789	2.278 ± 0.009	3281.00 ± 2.92	-0.049 ± 0.006	0.011 ± 0.025	10	1.40
NGC 5765b	3.727 ± 0.013	8314.64 ± 2.42	0.122 ± 0.008	-0.100 ± 0.034	10	1.15
NGC 6264	2.123 ± 0.007	10212.44 ± 3.50	0.005 ± 0.006	-	10	1.28
NGC 6323	0.917 ± 0.005	7840.72 ± 3.80	0.018 ± 0.007	0.013 ± 0.028	11	1.26
CGCG 074-064	2.750 ± 0.017	6946.32 ± 5.47	-0.040 ± 0.007	0.040 ± 0.020	11	1.27

Table 5.2: Posterior values of the fit. Column 1: Name of the megamaser system. Column 2: Fitted mass-to-distance ratio. Column 3: The Hubble constant times distance. Column 4: Horizontal offset (x_0) of the black hole found by the Bayesian fit. Column 5: Vertical offset (y_0) of the black hole found by the Bayesian fit. For NGC 6264 the y_0 offset is fixed at the geometric center of the disk formed by the high-redshifted maser features. Column 6: Scattering angle in which the maser features are spread on the azimuthal angle about the midline. Column 7: Reduced χ^2 of the best fit.

error in y_0. Nevertheless, this disk has a larger height, so the distribution along this axis makes the estimation on y more precise. Besides, the scale in y makes the errors in the y offset seem smaller.

5.2 Estimation with five galaxies

In this estimation we set the Gaussian prior $H_0 = 73.04 \pm 1.04$ km s^{-1} Mpc^{-1}, based on the estimation of this parameter from [50]. In this paper, the local value of the Hubble constant is measured using the Hubble Space Telescope and the SH0ES Team, where they use Cepheids and Type Ia Supernovae observations.

By using this Gaussian prior, we are able to estimate the parameters M, r_d and H_0 separately. The posterior result for the Hubble constant is $H_0 = 72.89^{+1.04}_{-1.03}$ km s^{-1} Mpc^{-1}, and its reduced Pearson's $\chi^2 = 1.27$.

System	M ($10^7 M_\odot$)	r_d Mpc	x_0 (mas)	y_0 (mas)	$\delta\phi$ (°)
UGC 3789	1.025 ± 0.015	$45.01^{+0.65}_{-0.63}$	-0.049 ± 0.006	0.011 ± 0.025	10
NGC 5765b	4.251 ± 0.063	$114.06^{+1.64}_{-1.60}$	0.122 ± 0.008	-0.100 ± 0.034	10
NGC 6264	2.978 ± 0.044	$140.09^{+2.01}_{-1.97}$	0.005 ± 0.006	-	10
NGC 6323	0.987 ± 0.015	$107.56^{+1.54}_{-0.04}$	0.018 ± 0.027	0.012 ± 1.512	11
CGCG 074-064	2.621 ± 0.041	$95.29^{+1.37}_{-1.34}$	-0.040 ± 0.006	0.039 ± 1.37	11

Table 5.3: Posterior values of the fit for the five galaxies. Column 1: Name of the megamaser system. Column 2: Fitted mass. Column 3: Estimated distance. Column 4: Horizontal offset (x_0). Column 5: Vertical offset (y_0). Column 6: Scattering angle.

The posterior results for the mass, distance, position and scattering angle for the five galaxies are shown in Table 5.3. The posterior probability distributions and the confidence regions for this estimation are shown in Figure 5.6. Note, in this Figure, the correlation between the five masses, distances and the Hubble constant. Such correlation is because the Hubble constant is correlated with the distance, since in our equations the term $H_0 r_d$ is always present. In addition, the mass and the distance are correlated given that we also have M/r_d in our equations. Therefore, given that we estimate H_0 using the data of the five galaxies altogether, the masses and distances of the galaxies all correlate between them.

5.3 Calculation of the gravitational and kinematic redshifts

Now, using the results presented in Table 5.2 of M/r_d, $H_0 r_d$ and the black hole position (x_0, y_0), we can calculate the gravitational and kinematic redshifts using equations (2.34) and (2.35), respectively. We calculate these redshifts for the closest maser feature to

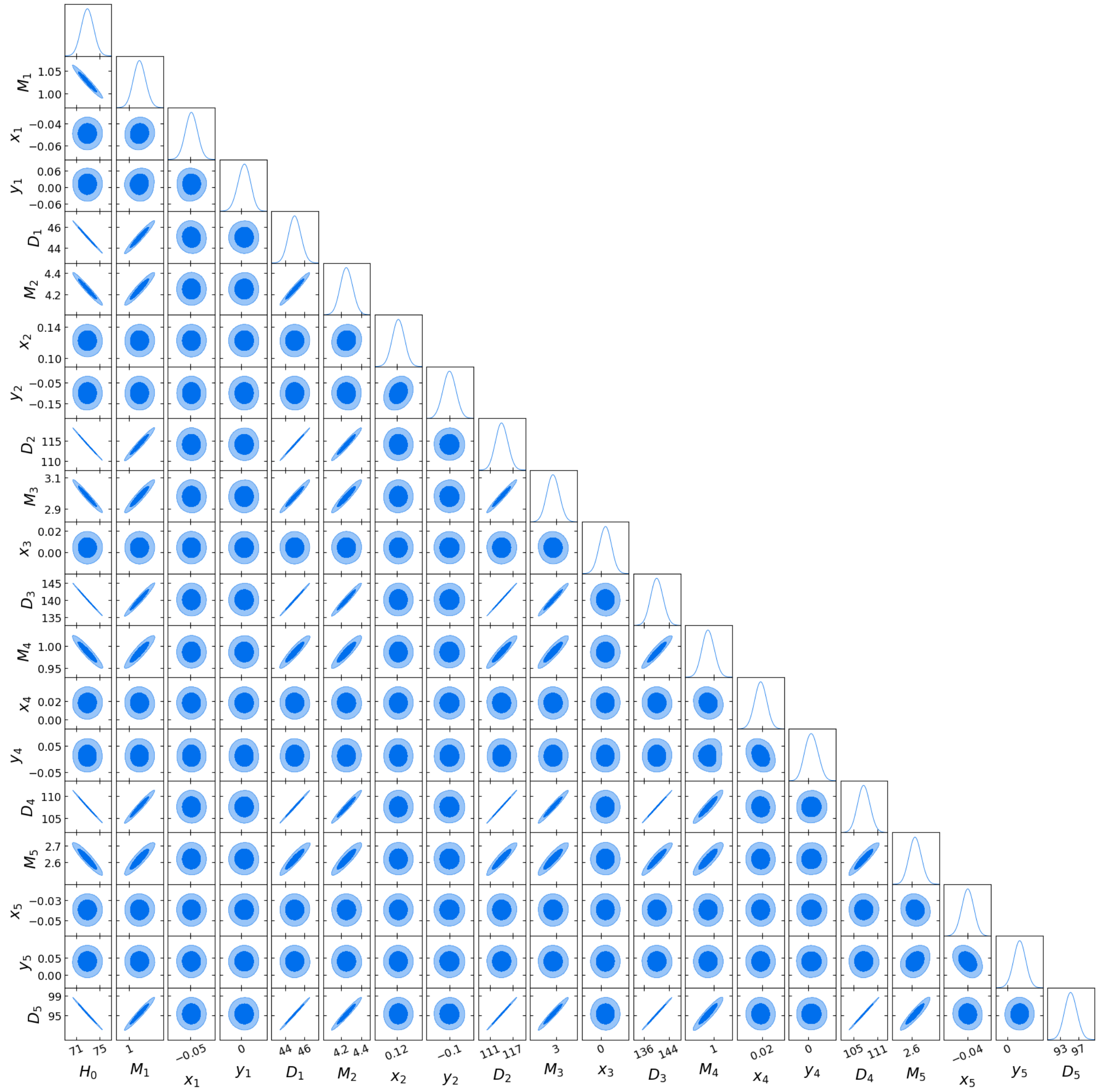

Figure 5.6: Posterior probability distributions and confidence regions for the parameters corresponding to the five galaxies.

Source	Distance to the closest maser (mas)	$cZ_{g,SdS}$ (km/s)	$cZ_{g,Schw}$ (km/s)	$cZ_{kin,SdS}$ (km/s)	$cZ_{kin,Schw}$ (km/s)
UGC 3789	0.305	3284.34	3.308	822.10	813.20
NGC 5765b	0.537	8317.80	3.076	805.88	784.13
NGC 6264	0.336	10215.34	2.805	774.30	748.79
NGC 6323	0.214	7842.65	1.893	631.31	615.22
CGCG 074-064	0.252	6951.26	4.832	1005.55	982.78

Table 5.4: Gravitational and kinematic redshift in terms of velocity for the full SdS case and the Schwarzschild case. Column 1: Name of the system. Column 2: Distance from the posterior black hole position to the closest maser feature. Column 3: Velocity associated to the SdS gravitational redshift. Column 4: Velocity associated to the Schwarzschild gravitational redshift. Column 5: Velocity associated to the SdS kinematic redshift. Column 6: Velocity associated to the Schwarzschild kinematic redshift.

the posterior black hole position, given that the values of the redshifts are higher for smaller r_e. We also compute the redshifts for the Schwarzschild case given by Equations (2.39) and (2.40) in order to compare these two models. These redshifts for each galaxy are shown in Table 5.4 in terms of velocity.

From these results, we can see that the SdS gravitational redshift is significantly bigger than the Schwarzschild case. This is because now we have the expansion embedded in the gravitational redshift, given that this gravitational redshift also depends on Λ. For the kinematic redshift, the results of both cases are quite similar, nevertheless, the kinematic redshift has also dependence on Λ. These results show us that most of the expansion is into the gravitational redshift.

Chapter 6

Discussion and conclusions

In this work, we have related the Hubble constant and black hole parameters to the observational frequency shift using a general relativistic formalism within the SdS background. We derived an expression for the redshift in term of these quantities, allowing us to relate the cosmological constant with the mass, distance and position of the black hole. The total redshift expression comprises two components: the gravitational redshift and the kinematic redshift, both depending on the black hole parameters and the cosmological constant. Unlike previous works, where the recessional motion of the system was considered as an additional composition to the Schwarzschild redshift (similar to Equation (2.36), see [45]), the SdS metric includes the redshift due to the cosmic expansion through the cosmological constant. This provides a more integrated description of the universe's expansion through redshift. Given that we recover the Hubble law in the approximation (2.41), we can say Equation (2.32) is a generalization of the Hubble law obtained from first principles of general relativity.

Regarding our fitting results, we estimated the mass-to-distance ratio M/r_d, the product $H_0 r_d$, and the black hole position (x_0, y_0) for five black holes using spectroscopy and astrometry data of the maser features on their accretion disks. By incorporating a Gaussian prior for the Hubble constant, we were able to disentangle these quantities and estimate the mass, distance and the Hubble constant separately. Our posterior results yielded black hole masses within the range $10^6 - 10^7$ $\mathrm{M}_\odot$, indicating that these black holes are supermassive, consistent with the hypothesis of existence of supermassive black holes in AGNs [66, 67]. Comparing the masses and distances of our estimations with those obtained by astronomers using a Newtonian model with relativistic corrections, we find that our results are in agreement with theirs (see the references mentioned in Table 5.1 for comparison with our results). Additionally, for the five systems, the estimated black hole positions (x_0, y_0) lie within the region of the systemic masers, which is physically in concordance with the maser emission mechanism.

Furthermore, the results in the computation of the SdS gravitational redshift indicate that the expansion is mostly embedded in this redshift, making the gravitational redshift no longer small, unlike in the Schwarzschild case, where this redshift is only due to the mass of the black hole and the order of its associated velocity is 1 km s^{-1}.

This work provides a first approximation for estimating the Hubble constant in a universe without matter dominated by dark energy, where the model depends only in redshift observations. In further works, we could decouple the quantities M/r_d and $H_0 r_d$ by modeling the maser disk and setting dependence on r_d. We wish to break such coupling in order to not rely on the Gaussian prior based on distance indicators, and therefore obtain an independent estimation of the Hubble constant based solely on general relativity and redshift observations.

Appendix A

Relativistic boost

We can compose the SdS redshift with a relativistic boost Z_{boost} in order to consider additional motion of the system not considered in the model. This motion may be the peculiar motion of the galaxy, which is due to local gravitational interactions and the proper motion of the galaxy. This relativistic boost reads

$$1 + Z_{boost} = \frac{1 + \beta \cos\alpha}{\sqrt{1 - \beta^2}}, \tag{A.1}$$

where $\beta \equiv v_{pec}/c$, v_{pec} is the peculiar motion of the galaxy, and α is the angle between the LOS and the direction of the peculiar velocity. In this manner, the term $v_{pec} \cos\alpha$ accounts for the radial motion of the galaxy. For simplicity, we continue the analysis considering the peculiar motion is purely radial, so $\alpha = 0$.

Thus, the redshift composition [68] renders a total redshift

$$Z_{tot_{1,2}} = (1 + Z_{SdS_{1,2}})(1 + Z_{boost}). \tag{A.2}$$

For the case of the peculiar motion, the velocities are less than 1% of the speed of light, so we could use $(1 + v_{pec}/c)$ instead of equation (A.1), but for the sake of using a completely relativistic model, we keep using this expression.

Appendix B

Full SdS expressions

In this Appendix we present the explicit formulas where the full redshift is used. The SdS redshift from Equation (2.32) reads

$$1+Z_{SdS_{1,2}} = \frac{1}{\sqrt{1-\frac{3M}{r_d\Theta}}}\left(1\pm\sqrt{\frac{\frac{M}{r_d\Theta}-(H_0r_d\Theta)^2}{1-\frac{2M}{r_d\Theta}-(H_0r_d\Theta)^2}}\right)\times$$

$$\frac{\left(1-\frac{2M}{r_d}-(H_0r_d)^2)\right)}{\sqrt{1-3(MH_0)^{2/3}}-\sqrt{\frac{2M}{r_d}+(H_0r_d)^2-3(MH_0)^{2/3}}\sqrt{1-\left(\frac{r_e}{r_d}\right)^2\frac{1-\frac{2M}{r_d}-(H_0r_d)^2}{1-\frac{2M}{r_d\Theta}-(H_0r_d\Theta)^2}}}. \tag{B.1}$$

Since in this case we have

$$1+Z_{SdS_{1,2}} = Z_{grav}+Z_{kin_{1,2}},$$

as in Equation (2.33), the reduced Pearson's χ^2 reads

$$\frac{\chi^2}{N}=\sum_{i=1}^{N}\frac{\left[Z_{obs,i}-(Z_{grav}+\varepsilon\sin\theta_0 Z_{kin_{1,2}})\right]^2}{\delta Z^2_{SdS}+\left(\beta Z_{kin_{1,2}}(1+Z_\Lambda)\right)^2}, \tag{B.2}$$

Tha variation of the SdS redshift is

$$\delta Z_{SdS}=\delta Z_{grav}\pm\varepsilon\sin\theta_0\delta Z_{kin}, \tag{B.3}$$

where the errors of the gravitational redshift δZ_{grav} and the kinematic redshift δZ_{kin} are

$$\delta Z_{grav} = -\frac{(1+Z_{grav})^2}{1-\dfrac{3M}{r_d\Theta}}\frac{\delta\Theta}{\Theta}\times$$
$$\left[\frac{3M}{2r_d\Theta\,(1+Z_{grav})} + \frac{\Theta^2\left(1-\dfrac{3M}{r_d\Theta}\right)^{3/2}}{1-\dfrac{2M}{r_d\Theta}-(H_0r_d\Theta)^2}\left(\sqrt{\frac{\dfrac{2M}{r_d}+(H_0r_d)^2-3(MH_0)^{2/3}}{1-\dfrac{\Theta^2(1-2M/r_d-(H_0r_d)^2)}{1-2M/(r_d\Theta)-(H_0r_d\Theta)^2}}}+\frac{M}{r_d\Theta}-(H_0r_d\Theta)^2\right)\right], \tag{B.4}$$

$$\delta Z_{kin} = \delta Z_{grav}\sqrt{\frac{\dfrac{M}{r_d\Theta}-(H_0r_d\Theta)^2}{1-\dfrac{2M}{r_d\Theta}-(H_0r_d\Theta)^2}} - Z_{kin}\frac{\delta\Theta}{\Theta}\left(\frac{\dfrac{M}{2r_d\Theta}+(H_0r_d\Theta)^2}{\dfrac{M}{r_d\Theta}-(H_0r_d\Theta)^2}+\frac{\dfrac{M}{r_d\Theta}-(H_0r_d\Theta)^2}{1-\dfrac{2M}{r_d\Theta}-(H_0r_d\Theta)^2}\right). \tag{B.5}$$

The expressions presented in this Appendix are the ones used in the Bayesian estimations.

Bibliography

[1] A. Einstein. “Zur Elektrodynamik bewegter Körper”. In: *Annalen der Physik* 322.10 (Jan. 1905), pp. 891–921. DOI: `10.1002/andp.19053221004`.

[2] A. Einstein. “Zur allgemeinen Relativitätstheorie”. In: *Sitzungsberichte der Koumlniglich Preussischen Akademie der Wissenschaften* (Jan. 1915), pp. 778–786.

[3] A. Einstein. “Erklärung der Perihelbewegung des Merkur aus der allgemeinen Relativitätstheorie”. In: *Sitzungsberichte der Koumlniglich Preussischen Akademie der Wissenschaften* (Jan. 1915), pp. 831–839.

[4] A. Einstein. “Die Feldgleichungen der Gravitation”. In: *Sitzungsberichte der Koumlniglich Preussischen Akademie der Wissenschaften* (Jan. 1915), pp. 844–847.

[5] K. Schwarzschild. “Über das Gravitationsfeld eines Massenpunktes nach der Einsteinschen Theorie”. In: *Sitzungsberichte der Koumlniglich Preussischen Akademie der Wissenschaften* (Jan. 1916), pp. 189–196.

[6] H. Reissner. “Über die Eigengravitation des elektrischen Feldes nach der Einsteinschen Theorie”. In: *Annalen der Physik* 355.9 (Jan. 1916), pp. 106–120. DOI: `10.1002/andp.19163550905`.

[7] G. Nordström. “On the Energy of the Gravitation field in Einstein’s Theory”. In: *Koninklijke Nederlandse Akademie van Wetenschappen Proceedings Series B Physical Sciences* 20 (Jan. 1918), pp. 1238–1245.

[8] F. Kottler. “Über die physikalischen Grundlagen der Einsteinschen Gravitationstheorie”. In: *Annalen der Physik* 361.14 (Jan. 1918), pp. 401–462. DOI: `10.1002/andp.19183611402`.

[9] E. Hubble. “A relation between distance and radial velocity among extra-galactic nebulae”. In: *Proceedings of the National Academy of Sciences* 15.3 (1929), pp. 168–173. DOI: `10.1073/pnas.15.3.168`.

[10] S. Chandrasekhar. “The Maximum Mass of Ideal White Dwarfs”. In: 74 (July 1931), p. 81. DOI: `10.1086/143324`.

[11] J. R. Oppenheimer and H. Snyder. “On Continued Gravitational Contraction”. In: *Phys. Rev.* 56 (5 Sept. 1939), pp. 455–459. DOI: `10.1103/PhysRev.56.455`. URL: `https://link.aps.org/doi/10.1103/PhysRev.56.455`.

[12] R. Penrose. “Gravitational Collapse and Space-Time Singularities”. In: *Phys. Rev. Lett.* 14 (3 Jan. 1965), pp. 57–59. DOI: `10.1103/PhysRevLett.14.57`. URL: `https://link.aps.org/doi/10.1103/PhysRevLett.14.57`.

[13] S. W. Hawking and R. Penrose. “The Singularities of Gravitational Collapse and Cosmology”. In: *Proceedings of the Royal Society of London Series A* 314.1519 (Jan. 1970), pp. 529–548. DOI: `10.1098/rspa.1970.0021`.

[14] K. A. Pounds et al. “X-ray reflection from cold matter in the nuclei of active galaxies”. In: *Nature* 344 (1990), pp. 132–133. DOI: `10.1038/344132a0`.

[15] J.M. Miller. “Relativistic X-Ray Lines from the Inner Accretion Disks Around Black Holes”. In: *Annual Review of Astronomy and Astrophysics* 45.Volume 45, 2007 (2007), pp. 441–479. ISSN: 1545-4282. DOI: `https://doi.org/10.1146/annurev.astro.45.051806.110555`. URL: `https://www.annualreviews.org/content/journals/10.1146/annurev.astro.45.051806.110555`.

[16] J. García, T. R. Kallman, and R. F. Mushotzky. “X-ray Reflected Spectra from Accretion Disk Models. II. Diagnostic Tools for X-ray Observations”. In: 731.2, 131 (Apr. 2011), p. 131. DOI: `10.1088/0004-637X/731/2/131`. arXiv: `1101.1115 [astro-ph.HE]`.

[17] LIGO Scientific Collaboration and Virgo Collaboration. “Observation of Gravitational Waves from a Binary Black Hole Merger”. In: 116.6, 061102 (Feb. 2016), p. 061102. DOI: `10.1103/PhysRevLett.116.061102`. arXiv: `1602.03837 [gr-qc]`.

[18] LIGO Scientific Collaboration and Virgo Collaboration. "GWTC-1: A Gravitational-Wave Transient Catalog of Compact Binary Mergers Observed by LIGO and Virgo during the First and Second Observing Runs". In: *Phys. Rev. X* 9.3, 031040 (July 2019), p. 031040. DOI: `10.1103/PhysRevX.9.031040`. arXiv: `1811.12907 [astro-ph.HE]`.

[19] Event Horizon Telescope Collaboration. "First M87 Event Horizon Telescope Results. I. The Shadow of the Supermassive Black Hole". In: 875.1, L1 (Apr. 2019), p. L1. DOI: `10.3847/2041-8213/ab0ec7`. arXiv: `1906.11238 [astro-ph.GA]`.

[20] Event Horizon Telescope Collaboration. "First M87 Event Horizon Telescope Results. IV. Imaging the Central Supermassive Black Hole". In: 875.1, L4 (Apr. 2019), p. L4. DOI: `10.3847/2041-8213/ab0e85`. arXiv: `1906.11241 [astro-ph.GA]`.

[21] Event Horizon Telescope Collaboration. "First M87 Event Horizon Telescope Results. VI. The Shadow and Mass of the Central Black Hole". In: 875.1, L6 (Apr. 2019), p. L6. DOI: `10.3847/2041-8213/ab1141`. arXiv: `1906.11243 [astro-ph.GA]`.

[22] Event Horizon Telescope Collaboration. "First Sagittarius A* Event Horizon Telescope Results. I. The Shadow of the Supermassive Black Hole in the Center of the Milky Way". In: 930.2, L12 (May 2022), p. L12. DOI: `10.3847/2041-8213/ac6674`.

[23] Event Horizon Telescope Collaboration. "First Sagittarius A* Event Horizon Telescope Results. III. Imaging of the Galactic Center Supermassive Black Hole". In: 930.2, L14 (May 2022), p. L14. DOI: `10.3847/2041-8213/ac6429`.

[24] R. Genzel and C. H. Townes. "Physical conditions, dynamics, and mass distribution in the center of the galaxy." In: 25 (Jan. 1987), pp. 377–423. DOI: `10.1146/annurev.aa.25.090187.002113`.

[25] R. Genzel et al. "The Dark Mass Concentration in the Central Parsec of the Milky Way". In: 472 (Nov. 1996), p. 153. DOI: `10.1086/178051`.

[26] A. M. Ghez et al. "High Proper-Motion Stars in the Vicinity of Sagittarius A*: Evidence for a Supermassive Black Hole at the Center of Our Galaxy". In: 509.2 (Dec. 1998), pp. 678–686. DOI: `10.1086/306528`. arXiv: `astro-ph/9807210 [astro-ph]`.

[27] A. M. Ghez et. al. "Stellar Orbits around the Galactic Center Black Hole". In: *The Astrophysical Journal* 620.2 (Feb. 2005), pp. 744–757. DOI: `10.1086/427175`.

[28] A. M. Ghez et. al. “Measuring Distance and Properties of the Milky Way’s Central Supermassive Black Hole with Stellar Orbits”. In: *The Astrophysical Journal* 689.2 (Dec. 2008), pp. 1044–1062. DOI: `10.1086/592738`.

[29] S. Gillessen et. al. “Monitoring Stellar Orbits Around the Massive Black Hole in the Galactic Center”. In: *The Astrophysical Journal* 692.2 (Feb. 2009), pp. 1075–1109. DOI: `10.1088/0004-637X/692/2/1075`.

[30] R. Genzel et. al. “The Galactic Center Massive Black Hole and Nuclear Star Cluster”. In: *Reviews of Modern Physics* 82.4 (Oct. 2010), pp. 3121–3195. DOI: `10.1103/RevModPhys.82.3121`.

[31] J. R. Herrnstein et. al. “The Geometry of and Mass Accretion Rate through the Maser Accretion Disk in NGC 4258”. In: *The Astrophysical Journal* 629.2 (Aug. 2005), pp. 719–738. DOI: `10.1086/431175`.

[32] E. M. L. Humphreys et. al. “Toward a New Geometric Distance to the Active Galaxy NGC 4258. III. Final Results and the Hubble Constant”. In: *The Astrophysical Journal* 775.1 (Sept. 2013), p. 13. DOI: `10.1088/0004-637X/775/1/13`.

[33] M. J. Reid et. al. “The Megamaser Cosmology Project. IV. A Direct Measurement of the Hubble Constant from UGC 3789”. In: *The Astrophysical Journal* 767.2 (2013), p. 154. DOI: `10.1088/0004-637X/767/2/154`.

[34] A. Herrera-Aguilar and U. Nucamendi. “Kerr black hole parameters in terms of the redshift/blueshift of photons emitted by geodesic particles”. In: *Physical Review D* 92 (4 Aug. 2015), p. 045024. DOI: `10.1103/PhysRevD.92.045024`. URL: `https://link.aps.org/doi/10.1103/PhysRevD.92.045024`.

[35] P. Banerjee et. al. “Mass and Spin of Kerr Black Holes in Terms of Observational Quantities: The Dragging Effect on the Redshift”. In: *Physical Review D* 105 (June 2022), p. 124037. DOI: `10.1103/PhysRevD.105.124037`.

[36] M. Momennia et. al. “Kerr black hole in de Sitter spacetime and observational redshift: Toward a new method to measure the Hubble constant”. In: *Phys. Rev. D* 107 (10 May 2023), p. 104041. DOI: `10.1103/PhysRevD.107.104041`. URL: `https://link.aps.org/doi/10.1103/PhysRevD.107.104041`.

[37] Gerardo Morales-Herrera et al. “Mass, charge, and distance to Reissner–Nordström black hole in terms of directly measurable quantities”. In: *Eur. Phys. J. C* 84.5 (2024), p. 525. DOI: `10.1140/epjc/s10052-024-12880-w`. arXiv: `2401.07112 [gr-qc]`.

[38] Diego A. Martinez-Valera, Mehrab Momennia, and Alfredo Herrera-Aguilar. “Observational redshift from general spherically symmetric black holes”. In: *Eur. Phys. J. C* 84.3 (2024), p. 288. DOI: `10.1140/epjc/s10052-024-12649-1`. arXiv: `2311.17993 [gr-qc]`.

[39] K. Y. Lo. “Mega-Masers and Galaxies”. In: *Annual Review of Astronomy and Astrophysics* 43.1 (Sept. 2005), pp. 625–676. DOI: `10.1146/annurev.astro.43.072103.150603`.

[40] M. Miyoshi et. al. “Evidence for a Black Hole from High Rotation Velocities in a Sub-parsec Region of NGC 4258”. In: *Nature* 373.6510 (Jan. 1995), pp. 127–129. DOI: `10.1038/373127a0`.

[41] J. R. Herrnstein et. al. “A Geometric Distance to the Galaxy NGC 4258 from Orbital Motions in a Nuclear Gas Disk”. In: *Nature* 400.6744 (Aug. 1999), pp. 539–541. DOI: `10.1038/22972`.

[42] C. Y. Kuo et. al. “The Megamaser Cosmology Project. III. Accurate Masses of Seven Supermassive Black Holes in Active Galaxies with Circumnuclear Megamaser Disks”. In: *The Astrophysical Journal* 727.1 (2011), p. 20. DOI: `10.1088/0004-637X/727/1/20`.

[43] F. Gao et. al. “The Megamaser Cosmology Project. IX. Black Hole Masses for Three Maser Galaxies”. In: *The Astrophysical Journal* 834 (Oct. 2016). DOI: `10.3847/1538-4357/834/2/111`.

[44] C. Y. Kuo et. al. “The Megamaser Cosmology Project XII. VLBI Imaging of H2O Maser Emission in Three Active Galaxies and the Effect of AGN Winds on Disc Dynamics”. In: *Monthly Notices of the Royal Astronomical Society* 498 (Sept. 2020), pp. 1609–1627. DOI: `10.1093/mnras/staa2327`.

[45] U. Nucamendi et. al. “Toward the Gravitational Redshift Detection in NGC 4258 and the Estimation of its Black Hole Mass-to-Distance Ratio”. In: *The Astrophysical Journal Letters* 917 (Aug. 2021), p. L14. DOI: `10.3847/2041-8213/ac0426`.

[46] A. Villalobos-Ramírez et. al. "A General Relativistic Estimation of the Black Hole Mass-to-Distance Ratio at the Core of TXS 2226-184". In: *Astronomy & Astrophysics* 662 (2022), p. L9. DOI: `10.1051/0004-6361/202243586`.

[47] D. Villaraos et. al. "A General Relativistic Mass-to-Distance Ratio for a Set of Megamaser AGN Black Holes". In: *Monthly Notices of the Royal Astronomical Society* 517.3 (2022), pp. 4213–4219. DOI: `10.1093/mnras/stab2628`.

[48] A. González-Juárez et al. "The mass-to-distance ratio for a set of megamaser AGN black holes by employing a general relativistic method". In: *To appear in Astronomy & Astrophysics* (2024). arXiv: `2211.06486 [astro-ph.GA]`.

[49] M. Kamionkowski and A. Riess. "The Hubble Tension and Early Dark Energy". In: *Ann. Rev. Nucl. Part. Sci.* 73 (2023), pp. 153–180. DOI: `10.1146/annurev-nucl-111422-024107`. arXiv: `2211.04492 [astro-ph.CO]`.

[50] A. G. Riess et al. "A Comprehensive Measurement of the Local Value of the Hubble Constant with 1 km s^{-1} Mpc^{-1} Uncertainty from the Hubble Space Telescope and the SH0ES Team". In: 934.1, L7 (July 2022), p. L7. DOI: `10.3847/2041-8213/ac5c5b`. arXiv: `2112.04510 [astro-ph.CO]`.

[51] Planck Collaboration. "Planck 2018 results. VI. Cosmological parameters". In: 641, A6 (Sept. 2020), A6. DOI: `10.1051/0004-6361/201833910`. arXiv: `1807.06209 [astro-ph.CO]`.

[52] M. J. Claussen and K. -Y. Lo. "Circumnuclear Water Vapor Masers in Active Galaxies". In: 308 (Sept. 1986), p. 592. DOI: `10.1086/164529`.

[53] L. J. Greenhill et al. "Centripetal acceleration within the subparsec nuclear maser disk of NGC4258." In: 304 (Dec. 1995), p. 21.

[54] L. J. Greenhill et al. "Detection of a Subparsec Diameter Disk in the Nucleus of NGC 4258". In: 440 (Feb. 1995), p. 619. DOI: `10.1086/175301`.

[55] N. Nakai, M. Inoue, and M. Miyoshi. "Extremely-high-velocity H_20 maser emission in the galaxy NGC4258". In: 361.6407 (Jan. 1993), pp. 45–47. DOI: `10.1038/361045a0`.

[56] J. M. Moran. "The Black Hole Accretion Disk in NGC 4258: One of Nature's Most Beautiful Dynamical Systems". In: *ASP Conf. Ser.* 395 (2008), p. 87. arXiv: `0804.1063 [astro-ph]`.

[57] M. J. Reid et al. "The Megamaser Cosmology Project: I. VLBI observations of UGC 3789". In: *Astrophys. J.* 695 (2009), pp. 287–291. DOI: `10.1088/0004-637X/695/1/287`. arXiv: `0811.4345 [astro-ph]`.

[58] C. Y. Kuo et al. "The Megamaser Cosmology Project. V. An Angular Diameter Distance to NGC 6264 at 140 Mpc". In: 767 (July 2012). DOI: `10.1088/0004-637X/767/2/155`.

[59] C. Y. Kuo et al. "The Megamaser Cosmology Project. VI. Observations of NGC 6323". In: 800 (Nov. 2014). DOI: `10.1088/0004-637X/800/1/26`.

[60] F. Gao et al. "The Megamaser Cosmology Project VIII. A Geometric Distance to NGC 5765b". In: 817 (Nov. 2015). DOI: `10.3847/0004-637X/817/2/128`.

[61] D. Pesce et al. "The Megamaser Cosmology Project. XI. A geometric distance to CGCG 074-064". In: 890 (Jan. 2020). DOI: `10.3847/1538-4357/ab6bcd`.

[62] M. P. Hobson et al., eds. *Bayesian Methods in Cosmology.* Cambridge: Cambridge University Press, 2009.

[63] B. J. Brewer. "Bayesian Inference and Computation: A Beginner's Guide". In: *Bayesian Astrophysics.* Ed. by A. Asensio Ramos and I. Arregui. 1st. Cambridge: Cambridge University Press, 2018. Chap. 1, pp. 1–10.

[64] Sivia D. and J. Skilling. *Data Analysis: A Bayesian Tutorial.* 2nd. Oxford: Oxford University Press, 2006. ISBN: 9780198568315.

[65] R. Schoot et al. "Bayesian statistics and modelling". In: *Nature Reviews Methods Primers* 1 (Dec. 2021). DOI: `10.1038/s43586-020-00001-2`.

[66] Martin J. Rees. "Black Hole Models for Active Galactic Nuclei". In: 22 (Jan. 1984), pp. 471–506. DOI: `10.1146/annurev.aa.22.090184.002351`.

[67] J. Kormendy and L. C. Ho. "Coevolution (Or Not) of Supermassive Black Holes and Host Galaxies". In: 51.1 (Aug. 2013), pp. 511–653. DOI: `10.1146/annurev-astro-082708-101811`. arXiv: `1304.7762 [astro-ph.CO]`.

[68] T. M. Davis and M. I. Scrimgeour. "Deriving accurate peculiar velocities (even at high redshift)". In: *Monthly Notices of the Royal Astronomical Society* 442.2 (June 2014), pp. 1117–1122. ISSN: 0035-8711. DOI: `10.1093/mnras/stu920`. eprint: `https:`

`//academic.oup.com/mnras/article-pdf/442/2/1117/5749233/stu920.pdf`. URL: `https://doi.org/10.1093/mnras/stu920`.